

Parallel adaptive weakly-compressible SPH for complex moving geometries

Asmelash Haftu^{a,*}, Abhinav Muta^a, Prabhu Ramachandran^a

^a*Department of Aerospace Engineering, Indian Institute of Technology Bombay, Powai, Mumbai 400076*

Abstract

The use of adaptive spatial resolution to simulate flows of practical interest using Smoothed Particle Hydrodynamics (SPH) is of considerable importance. Recently, Muta and Ramachandran [1] have proposed an efficient adaptive SPH method which is capable of handling large changes in particle resolution. This allows the authors to simulate problems with much fewer particles than was possible earlier. The method was not demonstrated or tested with moving bodies or multiple bodies. In addition, the original method employed a large number of background particles to determine the spatial resolution of the fluid particles. In the present work we establish the formulation's effectiveness for simulating flow around stationary and moving geometries. We eliminate the need for the background particles in order to specify the geometry-based or solution-based adaptivity and we discuss the algorithms employed in detail. We consider a variety of benchmark problems, including the flow past two stationary cylinders, flow past different NACA airfoils at a range of Reynolds numbers, a moving square at various Reynolds numbers, and the flow past an oscillating cylinder. We also demonstrate different types of motions using single and multiple bodies. The source code is made available under an open source license, and our results are reproducible.

Keywords: Adaptive spatial resolution, Incompressible flow, Moving

*Corresponding author

Email addresses: asmelash.a@aero.iitb.ac.in (Asmelash Haftu), abhinavm@aero.iitb.ac.in (Abhinav Muta), prabhu@aero.iitb.ac.in (Prabhu Ramachandran)

geometries, Multi body simulation, Smoothed Particle Hydrodynamics.

Program Summary

Program Title: Parallel adaptive EDAC-SPH

CPC Library link to program files: (to be added by Technical Editor)

Developer's repository link: https://gitlab.com/pypr/asph_motion.

Code Ocean capsule: (to be added by Technical Editor)

Licensing provisions: BSD 3-clause

Programming language: Python

External routines/libraries: PySPH (<https://github.com/pypr/pysph>), matplotlib (<https://pypi.org/project/matplotlib/>), NumPy (<https://pypi.org/project/numpy/>), automan (<https://pypi.org/project/automan/>), compyle (<https://pypi.org/project/compyle/>).

Nature of problem: Simulating fluid flow around multiple moving bodies requires the local resolution to be automatically adapted in order to capture all the necessary flow features. If a single resolution is used throughout the domain, the number of particles would be excessively large.

Solution method: We validate and demonstrate the accuracy of the adaptive particle refinement algorithm in simulating flow past moving multiple geometries. Our algorithm is fully parallel, and we provide an open-source implementation.

1. Introduction

The study of fluid flows in complex scenarios is immensely important in science and engineering. Problems involving multiple bodies, thin structures, and moving or deforming boundaries are a few examples of interest. For the simulation of such systems, the mesh-based approach of computational fluid dynamics (CFD) faces issues due to mesh distortion [2, 3] in addition to the expertise and the considerable amount of time required for good quality meshing. An alternative to mesh-based approaches is to use meshless particle methods, particularly Smoothed Particle Hydrodynamics (SPH). SPH is a Lagrangian, mesh-free method that employs particles to discretize the fluid, the combined motion of which is analogous to the flow of gases or liquids [4, 5]. SPH is suitable for complex dynamics with multi-body and multi-motion simulation, innately allowing simplified geometry description for such problems. Most importantly, it allows dynamic adaptive particle resolution

[6, 7]. It has so far shown a significant headway that its desirability is apparent from the increasingly large number of published works, simulation packages, and range of applications. Since the initial application in astrophysics [8, 9], SPH has been widely studied and broadly applied to problems in the areas of fluid mechanics [10, 11, 12, 13, 14], solid mechanics [15, 16], and fluid-structure interactions [17, 18]. The range of applications studied also cover fields in hydrodynamics [19, 20], multiphase flows [21, 22], free-surface flows [23, 24], turbulence [19, 25, 26], atomization in combustion [27, 28], food industries [29], and many other areas. The grand challenges (GC) in SPH have been discussed in detail by Vacondio et al. [5] and Lind et al. [4]. In the present work, we consider the robust application of adaptive particle refinement/resolution (GC3), and SPH range of applicability (GC5).

Martel et al. [30] introduced adaptive particle resolution in SPH for cosmological simulation and treatment of shocks. Kitsionas and Whitworth [31] simulated a collapse of self-gravitating fluid by splitting particles to increase the resolution in high density localities. Lastiwka et al. [32] discussed an SPH framework for inserting and removing particles adaptively, and the accuracy achieved by the method was studied using a shock tube test case. Reyes Lopez and Roose [33] investigated a dynamic refinement scheme applicable to free surface as well as non-cohesive soil problems. In a separate study, López et al. [34] presented a dynamic particle refinement method for SPH in which they refine the particles by replacing them with smaller daughter particles. In a paper by Spreng et al. [35], a local adaptive discretization algorithm was presented for improving the accuracy of SPH simulations while reducing both time and cost of computation. This involves a combination of refinement and coarsening, which increases particles adaptively for areas of high interest in the domain and reduces in regions with lower interest. A particle refinement and coarsening method is discussed by Barcarolo et al. [36] in which one parent particle was split into four child particles of equal mass within the refinement zone and recombined after leaving the refinement zone. The total mass was not found conserved at all times during the operation. Khorasanizade and Sousa [37] illustrated the particle splitting technique using a dynamic approach. Adaptive mesh refinement of finite volume based CFD methods motivated García-Senz et al. [38] to create adaptive refinement of the particle in SPH by using guard particles to separate the zones with different levels of refinement. More studies related to adaptive particle refinement can be found in [39, 40, 41].

Feldman and Bonet [42] illustrated a dynamic particle refinement method and studied the error generated as a result of particle splitting. Candidate particles are identified and the original particle is split into seven smaller particles for which mass distribution is optimized through nonlinear minimization. The daughter particles are moved with the velocity of the original particle to conserve flow properties. Vacondio et al. [43] presented a variable resolution approach for splitting and merging SPH particles and simulating the Navier-Stokes (NS) equations. The particle sizes are dynamically modified by splitting and coalescing procedures of individual particles to achieve the required resolution in targeted zones. The adaptive algorithm for particles of variable smoothing lengths is implemented in an SPH scheme derived using a variational method ([44] and [45]) to ensure the conservation of mass and momentum. In this method, one parent particle was split into seven child particles during the refinement phase, whereas while coarsening, two-child particles were merged into one parent particle. The anisotropy and non-uniformity of particle distributions are controlled and generalized using particle shifting variable mass particles. The splitting accuracy was demonstrated for two-dimensional cases. Yang and Kong [21] developed an adaptive particle refinement technique for multiphase flows; defined criteria for the spacing of a reference particle which changes dynamically along with the location of the interface. The adaptive resolution was used with a smoothing length which also varied during the simulation. The smoothing length is considered variable because the spacing between particles is not uniform and it is averaged for the neighboring particles to reduce numerical errors. Refining and coarsening of fluid particles are carried out via splitting and merging techniques respectively. Near the interface, the particles are refined whereas, far away from the interface the particles are coarsened.

Many issues with adaptive SPH have been addressed in the recent work of Muta and Ramachandran [1]. Specifically, the method is accurate, efficient, supports multiple bodies, supports moving geometries, is automatically adaptive, and supports both geometry-based as well as solution-based adaptivity. In the original paper, the authors did not demonstrate any moving geometry problems or consider multiple bodies. The original method also employs background particles in order to set the particle resolution of the fluid particles. The number of particles used for the background is typically the same order as the fluid particles. This increases the complexity of the method and also increases its memory usage.

In this work, we demonstrate the applications of the adaptive SPH method of Muta and Ramachandran [1] for simulation of complex cases involving stationary and moving geometries. We also eliminate the need for the background particles and this reduces the complexity of the method, simplifies its implementation, and reduces the memory usage of the method. The method is proposed for the simulations of incompressible and weakly compressible fluid flows employing the Entropically Damped Artificial Compressibility (EDAC) formulation [46]. The adaptive resolution is fully automatic and produces an optimal mass distribution of particles and is accurate for the benchmark problems considered. It is based on methods developed by [21, 42, 43, 47, 48], with additional improvements. The refinement method elegantly allows static regions of refinement, geometry-based automatic refinement, and solution-based automatic adaptivity. The SPH method has not been extensively applied to problems that involve the motion of solids in a fluid medium at high resolution. Fortunately, moving or stationary solid bodies can be easily simulated at a range of Reynolds numbers using the aforementioned approach.

The main goals of this paper are to, (i) validate the adaptive EDAC-SPH method without the use of background particle by testing on incompressible flows at a range of Reynolds numbers, (ii) apply the method to moving geometries, (iii) apply it to complex geometries. We first simulate flow past two stationary cylinders at different gap spacing between the cylinders. We then perform flow simulation over stationary airfoils of narrow cross-section at a range of Reynolds numbers to illustrate the robustness of the method. Next, we show the flow around a moving square and cylinder for Reynolds numbers 50 – 600 and compare the results with established methods. We also apply the present model and simulate an oscillating single circular cylinder for different amplitudes and frequencies of oscillation. At the end we demonstrate different complex motions and multi-body simulations.

We provide an open-source implementation based on the PySPH framework [49]. The source code can be obtained from https://gitlab.com/pypr/asph_motion. The manuscript is reproducible and each figure is automatically generated through the use of an automation framework [50].

2. Smoothed particle hydrodynamics formulation

The governing equations for the viscous, weakly-compressible fluid flows using the entropically damped artificial compressibility (EDAC) formulation [51, 46],

written in transport velocity formulation [52], including the corrections terms of [53] involves two equations, one for the pressure evolution which is given as,

$$\frac{\tilde{d}p}{dt} = -\rho c_s^2 \text{div}(\mathbf{u}) + \nu_e \nabla^2 p + (\tilde{\mathbf{u}} - \mathbf{u}) \cdot \nabla p, \quad (1)$$

where p is the pressure, t is the time, ρ is the density, c_s is the artificial speed of sound, $\tilde{\mathbf{u}}$ is the transport velocity. $\frac{\tilde{d}(\cdot)}{dt} = \frac{\partial(\cdot)}{\partial t} + \tilde{\mathbf{u}} \cdot \text{grad}(\cdot)$ is the material time derivative of a particle advecting with the transport velocity $\tilde{\mathbf{u}}$, \mathbf{u} is the fluid velocity, and ν_e is the EDAC viscosity parameter. The second equation is the momentum equation, which is given as,

$$\frac{\tilde{d}\mathbf{u}}{dt} = -\frac{1}{\rho} \nabla p + \nu \nabla^2 \mathbf{u} + \mathbf{f} + \frac{1}{\rho} \nabla \cdot \rho(\mathbf{u} \otimes (\tilde{\mathbf{u}} - \mathbf{u})) + \mathbf{u} \text{div}(\tilde{\mathbf{u}}), \quad (2)$$

where ν is the kinematic viscosity of the fluid, and \mathbf{f} is the external body force. The positions \mathbf{r} of the Lagrangian fluid particles are updated using,

$$\frac{d\mathbf{r}}{dt} = \tilde{\mathbf{u}}. \quad (3)$$

We discretize the above governing equations using the variable- h SPH formulation [11, 47]. In the following the subscripts i and j denote the index of the particles in the discretized domain and the summation is taken over all the indices in the neighborhood of i^{th} particle. For the computation of the density ρ_i of a particle we use the gather form of summation density [54, 47],

$$\rho_i = \rho(\mathbf{r}_i) = \sum_j m_j W(r_{ij}, h_i), \quad (4)$$

where $W(r_{ij}, h_i) = W(|\mathbf{r}_i - \mathbf{r}_j|, h_i)$ is the kernel function, and h_i the smoothing length. We use the quintic spline kernel [12] in all our simulations, which is given by,

$$W(q) = \begin{cases} \sigma_2[(3-q)^5 - 6(2-q)^5 + 15(1-q)^5] & \text{if } 0 \leq q < 1, \\ \sigma_2[(3-q)^5 - 6(2-q)^5] & \text{if } 1 \leq q < 2, \\ \sigma_2(3-q)^5 & \text{if } 2 \leq q < 3, \\ 0 & \text{if } q \geq 3, \end{cases} \quad (5)$$

where $\sigma_2 = 7/(478\pi h(\mathbf{r})^2)$, and $q = |\mathbf{r}|/h$. The EDAC pressure evolution equation is given by,

$$\begin{aligned} \frac{\tilde{d}p}{dt}(\mathbf{r}_i) = & \frac{\rho_0 c_s^2}{\beta_i} \sum_j \frac{m_j}{\rho_j} \mathbf{u}_{ij} \cdot \nabla W(r_{ij}, h_i) \\ & + \frac{1}{\beta_i} \sum_j \frac{m_j}{\rho_j} \nu_{e,ij} (p_i - p_j) (\mathbf{r}_{ij} \cdot \nabla W(r_{ij}, h_{ij})) \\ & + \sum_j m_j [(\tilde{\mathbf{u}}_i - \mathbf{u}_i) \cdot (P_i \nabla W(r_{ij}, h_i) + P_j \nabla W(r_{ij}, h_j))], \end{aligned} \quad (6)$$

where ρ_0 is the reference density, $\mathbf{u}_{ij} = \mathbf{u}_i - \mathbf{u}_j$, β_i is the additional term obtained while deriving the variable- h formulation [47], which in d dimensions is given by,

$$\beta_i = -\frac{1}{\rho_i d} \sum_j m_j r_{ij} \frac{dW(r_{ij}, h_i)}{dr_{ij}}, \quad (7)$$

P_i and P_j , employing the pressure reduction technique [55] by removing the averaged pressure $p_{\text{avg},i} = \sum_j p_j / N_i$, are given by,

$$P_i = \frac{(p_i - p_{\text{avg},i})}{\rho_i^2 \beta_i}, \quad P_j = \frac{(p_j - p_{\text{avg},j})}{\rho_j^2 \beta_j}, \quad (8)$$

and the averaged gradient of the kernel is given by,

$$\nabla W(r_{ij}, h_{ij}) = \left(\frac{\nabla W(r_{ij}, h_i) + \nabla W(r_{ij}, h_j)}{2} \right). \quad (9)$$

For pressure diffusion term in the EDAC equation we use the formulation of Cleary and Monaghan [56] to discretize the coefficient $\nu_{e,ij}$ as,

$$\nu_{e,ij} = 4 \frac{\nu_{e,i} \nu_{e,j}}{(\nu_{e,i} + \nu_{e,j})}, \quad (10)$$

where the EDAC viscosity $\nu_{e,i}$, which is varying in space due to the presence of h_i , is discretized as [46],

$$\nu_{e,i} = \frac{\alpha_e c_s h_i}{8}, \quad (11)$$

where $\alpha_e = 1.5$ is used in all our simulations.

The momentum equation in the variable- h SPH discretization is given by,

$$\begin{aligned} \frac{d\mathbf{u}}{dt}(\mathbf{r}_i, t) = & - \sum_j m_j ((P_i + A_i) \nabla W(r_{ij}, h_i) + (P_j + A_j) \nabla W(r_{ij}, h_j)) \\ & + \frac{1}{\beta_i} \sum_j m_j \frac{4\nu}{(\rho_i + \rho_j)} \frac{\mathbf{r}_{ij} \cdot \nabla W(r_{ij}, h_{ij})}{(|\mathbf{r}_{ij}|^2 + \eta)} \mathbf{u}_{ij} \\ & - \frac{1}{\beta_i} \sum_j \frac{m_j}{\rho_j} [(\tilde{\mathbf{u}}_{ij} - \mathbf{u}_{ij}) \cdot \nabla W(r_{ij}, h_i)] \mathbf{u}_i, \end{aligned} \quad (12)$$

where,

$$A_i = \frac{1}{\rho_i \beta_i} \mathbf{u}_i \otimes (\tilde{\mathbf{u}}_i - \mathbf{u}_i), \quad A_j = \frac{1}{\rho_j \beta_j} \mathbf{u}_j \otimes (\tilde{\mathbf{u}}_j - \mathbf{u}_j), \quad (13)$$

and $\eta = 0.001h_i^2$ is a small number added to ensure a non-zero denominator in case when $i = j$. All our simulations are viscous and we do not employ any artificial viscosity.

We employ the shifting technique of Lind et al. [57], additionally limiting the particle movement if it shifts by more than 25% of its smoothing length, to ensure uniformity, leading to stable and accurate simulations [58, 57, 59]. Rather than shifting the particles directly, since we are using the transport velocity formulation, we incorporate the shifting into the computation of the transport velocity as,

$$\tilde{\mathbf{u}}_i = \mathbf{u}_i + \theta \frac{\delta \mathbf{r}_i}{\Delta t}, \quad (14)$$

where,

$$\delta \mathbf{r}_i = -\frac{h_i^2}{2} \sum_j \frac{m_j}{\rho_0} \left(1 + 0.24 \left(\frac{W(r_{ij}, h_{ij})}{W(\Delta x, \xi h_{ij})} \right)^4 \right) \nabla W_{ij}, \quad (15)$$

where $\xi = 0.759298480738450$ is the point of inflection of the quintic spline kernel [60], and $h_{ij} = (h_i + h_j)/2$; and,

$$\theta = \begin{cases} \frac{0.25h_i}{|\delta \mathbf{r}_i|} & \text{if } |\delta \mathbf{r}_i| > 0.25h_i, \\ 1 & \text{otherwise.} \end{cases} \quad (16)$$

2.1. Boundary conditions

We use the dummy particle approach of Adami et al. [61] to enforce the boundary conditions. We enforce no-penetration by using the wall velocity for the dummy particles in the EDAC equation. We enforce the no-slip and free-slip boundary condition by, first, extrapolating the fluid velocity onto the dummy particles using Shepard interpolation:

$$\hat{\mathbf{u}}_i = \frac{\sum_j \mathbf{u}_j W(r_{ij}, h_{ij})}{\sum_j W(r_{ij}, h_{ij})}, \quad (17)$$

where j is the index of the fluid particles in the neighborhood of the i^{th} dummy particle; then, the velocity of the dummy particles is computed from,

$$\mathbf{u}_w = 2\mathbf{u}_i - \hat{\mathbf{u}}_i, \quad (18)$$

where the subscript w denotes the dummy wall particles, \mathbf{u}_i is the prescribed wall velocity. To impose the pressure gradient accurately near the wall, the pressure on the dummy wall particles is computed by,

$$p_w = \frac{\sum_f p_f W(r_{wf}, h_{wf}) + (\mathbf{g} - \mathbf{a}_w) \cdot \sum_f \rho_f \mathbf{r}_{wf} W(r_{wf}, h_{wf})}{\sum_f W(r_{wf}, h_{wf})}, \quad (19)$$

where the subscript f denotes the fluid particles, \mathbf{a}_w is the acceleration of the wall, g is the acceleration due to gravity (this is zero in the present work), $r_{wf} = |\mathbf{r}_w - \mathbf{r}_f|$, and $h_{wf} = (h_w + h_f)/2$.

We use the no-reflection boundary conditions on the inviscid wall of all simulations. For this we use the approach of Lastiwka et al. [62], where we compute the characteristic properties, J_1 , J_2 , and J_3 , op. cit., from the fluid and extrapolate these properties onto the dummy particles describing the boundary using Shepard interpolation, finally, the fluid properties on the dummy particles are set from these characteristic properties.

2.2. Force computation

The forces due to the pressure and viscosity of the fluid on the solid are computed by evaluating,

$$\mathbf{f}^{\text{solid}} = m^{\text{solid}} \left(-\frac{1}{\rho} \nabla p + \nu \nabla \cdot \nabla \mathbf{u} \right), \quad (20)$$

which in the variable- h SPH discretization is written as,

$$\begin{aligned} \mathbf{f}_i^{\text{solid}} = & - \underbrace{m_i^{\text{solid}} \left[\sum_j m_j (P_i \nabla W(r_{ij}, h_i) + P_j \nabla W(r_{ij}, h_j)) \right]}_{\mathbf{f}_{i,p}} \\ & + \underbrace{m_i^{\text{solid}} \left[\frac{1}{\beta_i} \sum_j m_j \frac{4\nu}{(\rho_i + \rho_j)} \frac{\mathbf{r}_{ij} \cdot \nabla W(r_{ij}, h_{ij})}{(|\mathbf{r}_{ij}|^2 + \eta)} \mathbf{u}_{ij} \right]}_{\mathbf{f}_{i,\text{visc}}} \end{aligned} \quad (21)$$

where the summation index j is over all the fluid particles in the neighborhood of a i^{th} dummy particle. The drag C_d , lift C_l , and pressure C_p coefficients used for comparison of our results with reference data are expressed by:

$$C_d = \frac{(\mathbf{f}_p + \mathbf{f}_{\text{visc}}) \cdot \mathbf{e}_x}{0.5\rho_0 U_\infty^2 D}, \quad C_l = \frac{(\mathbf{f}_p + \mathbf{f}_{\text{visc}}) \cdot \mathbf{e}_y}{0.5\rho_0 U_\infty^2 D}, \quad C_p = \frac{p}{0.5\rho_0 U_\infty^2 D}, \quad (22)$$

where U_∞ is free-stream velocity of the fluid, \mathbf{e}_x and \mathbf{e}_y are the unit vectors in the x and y directions, respectively, $\mathbf{f}_p + \mathbf{f}_{\text{visc}} = \sum_j \mathbf{f}_{j,p} + \mathbf{f}_{j,\text{visc}}$ is the sum of all forces of the dummy particles, and D is the characteristic length.

2.3. Time integration

We use the Predict-Evaluate-Correct (PEC) integrator to integrate the position, velocity, and pressure. First, we predict the properties at an intermediate time $n + \frac{1}{2}$ by,

$$\mathbf{u}_i^{n+\frac{1}{2}} = \mathbf{u}_i^n + \frac{\Delta t}{2} \frac{d\mathbf{u}_i^n}{dt}, \quad (23)$$

$$\tilde{\mathbf{u}}_i^{n+\frac{1}{2}} = \mathbf{u}_i^{n+\frac{1}{2}} + \frac{\delta \mathbf{r}_i^n}{\Delta t}, \quad (24)$$

$$\mathbf{r}_i^{n+\frac{1}{2}} = \mathbf{r}_i^n + \frac{\Delta t}{2} \tilde{\mathbf{u}}_i^{n+\frac{1}{2}}, \quad (25)$$

$$p_i^{n+\frac{1}{2}} = p_i^n + \frac{\Delta t}{2} \frac{dp_i^n}{dt}, \quad (26)$$

next, we evaluate the rate of change of properties at $n + \frac{1}{2}$, then, we correct the properties to get the corresponding values at the new time $n + 1$ by,

$$\mathbf{u}_i^{n+1} = \mathbf{u}_i^n + \Delta t \frac{d\mathbf{u}_i^{n+\frac{1}{2}}}{dt}, \quad (27)$$

$$\tilde{\mathbf{u}}_i^{n+1} = \mathbf{u}_i^{n+1} + \frac{\delta \mathbf{r}_i^{n+\frac{1}{2}}}{\Delta t}, \quad (28)$$

$$\mathbf{r}_i^{n+1} = \mathbf{r}_i^n + \Delta t \tilde{\mathbf{u}}_i^{n+1}, \quad (29)$$

$$p_i^{n+1} = p_i^n + \Delta t \frac{d\mathbf{p}_i^{n+\frac{1}{2}}}{dt}. \quad (30)$$

The time-step is determined by the highest resolution used in the domain, and the minimum of the Courant–Friedrichs–Lewy (CFL) criterion and the viscous condition is taken:

$$\Delta t = \min \left(0.25 \left(\frac{h_{\min}}{U + c_s} \right), 0.125 \left(\frac{h_{\min}^2}{\nu} \right) \right). \quad (31)$$

3. Adaptive refinement

We discuss the adaptive refinement algorithm here. The present algorithm is based on the work of Muta and Ramachandran [1] in which the authors employ a collection of background particles in order to determine the spatial resolution of the fluid particles. The number of background particles is typically the same size as the number of fluid particles and these do not contribute significantly to the computation but do increase the memory required by the algorithm and also increase the complexity of the implementation. In the present work, we eliminate the background particles altogether. The algorithms discussed here are thus slightly different from the ones in [1].

Initially, we discretize all the solid bodies at the highest desired resolution, and set a parameter Δs_{\min} to this resolution. For complex bodies a particle packing algorithms [63] can be used to discretize at the desired resolution. We define two other parameters, Δs_{\max} the coarsest resolution in the domain, and $C_r = \frac{\Delta s_{k+1}}{\Delta s_k}$, the particle spacing ratio [21] between adjacent regions of refinement. The spacing ratio C_r controls the width of the refinement regions and is generally between 1.05 and 1.2.

We base our discussion on problems where solid bodies, stationary or moving, are placed in a wind-tunnel-like setup with fluid streaming between the inlet

and outlet. Once the domain size is specified, we iterate over all the fluid particles and mark the fluid particles which are in the neighborhood of the particles defining the solid bodies; we use a simple integer mask to achieve this. After fluid particles near the boundaries are identified, we iterate over the rest of the particles and find the minimum (Δs_{\min}), maximum (Δs_{\max}), and geometric mean (Δs_{avg}) of the Δs in the neighborhood of each particle. If $\Delta s_{\max}/\Delta s_{\min} < C_r^3$ we set the value of Δs to $C_r\Delta s_{\min}$. If $\Delta s_{\max}/\Delta s_{\min} \geq C_r^3$, we set $\Delta s = \Delta s_{\text{avg}}$. This immediately defines the reference $m_{\text{ref}} = \rho(\Delta s)^d$, minimum $m_{\min} = 0.5m_{\text{ref}}$ and maximum $m_{\max} = 1.05m_{\text{ref}}$ mass. Algorithm 1 shows the outline of this procedure.

Algorithm 1 Update spacing of particles

```

1: Define  $\Delta s$  for all particles
2: for all  $i$  of particles which are not fixed do
3:   find neighbors of  $i$ 
4:   find  $\Delta s_{\min}$ , and  $\Delta s_{\max}$  in the neighborhood
5:   find average spacing  $\Delta s_{\text{avg}}$  in the neighborhood
6:   if  $\frac{\Delta s_{\max}}{\Delta s_{\min}} < (C_r)^3$  then
7:      $h_{\text{tmp}} \leftarrow \min(\Delta s_{\max}, C_r\Delta s_{\min})$ 
8:   else
9:      $h_{\text{tmp}} \leftarrow \Delta s_{\text{avg}}$ 
10: for all  $i$  of particles which are not fixed do
11:    $m_i \leftarrow \rho_i h_{\text{tmp}}^2$ 
12:    $m_{i,\max} \leftarrow 1.05m_i$     $m_{i,\min} \leftarrow 0.5m_i$ 

```

Algorithm 2 describes the splitting procedure which follows Feldman and Bonet [42] and Vacondio et al. [47]. Figure 1 shows an illustration of the splitting algorithm. The orange hexagonal particles indicate the outer boundary or the edge of the fixed internal domain, the black square particles correspond to solid particles. Both the orange hexagonal and the black square particles constitute the fixed particles and will not subdivide. The blue particles correspond to the fluid particles and are non-fixed as they may subdivide. The green zone indicates the region having maximum mass $m_{\max} = m/2$. If a particle exceeds its maximum mass, we split the particle into 7 *daughter* particles, where we place 6 daughter particles on the vertices of a hexagon, at a distance of $\epsilon = 0.4$ times the smoothing length away from the original particle, centered around the location of the original particle. We place the

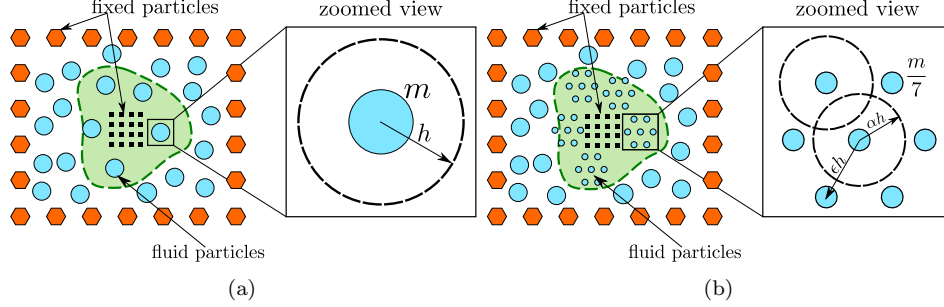


Figure 1: Illustration of the splitting algorithm (a) before the split, and (b) after the split. The particles outside the green zone have mass m and the maximum mass is $m_{\max} = m$. All the particles inside the green region have maximum mass $m_{\max} = m/2$. After the split the particles undergo merging which is not illustrated.

Algorithm 2 Splitting of the particles.

```

1:  $\epsilon \leftarrow 0.4$    $\alpha \leftarrow 0.9$ 
2: for all  $i$  of particles which are not fixed do
3:   if  $m_i > m_{i,\max}$  then
4:     split particle  $i$  to 7 daughters
5:     for  $k = 0; k < 7; k++$  do
6:        $m_{i,k} \leftarrow \frac{m_i}{7}, \quad h_{i,k} \leftarrow \alpha h_i$ 
7:        $\mathbf{u}_{i,k} \leftarrow \mathbf{u}_i, \quad \tilde{\mathbf{u}}_{i,k} \leftarrow \tilde{\mathbf{u}}_i$ 
8:        $p_{i,k} \leftarrow p_i, \quad \rho_{i,k} \leftarrow \rho_i$ 
9:        $\mathbf{x}_{i,0} \leftarrow \mathbf{x}_i$ 
10:      for  $k = 1; k < 7; k++$  do
11:         $\mathbf{x}_{i,k} \leftarrow \mathbf{x}_i + \epsilon h_i \cos\left(\frac{k\pi}{3}\right)$ 

```

7th daughter particle at the location of the original particle. The daughter particles' smoothing length is set to $\alpha = 0.9$ times that of the original particle smoothing length.

The merging algorithm follows Vacondio et al. [43] although with some differences that allow us to perform this in parallel. In a single iteration, a particle may merge only with one other particle. Two particles merge if the distance between the two is less than the mean smoothing length of the two $r_{ij} < (h_i + h_j)/2$, and the sum of mass of the two particles is less than the maximum of the m_{\max} of either of the particles $(m_i + m_j) < \max(m_{\max}[i], m_{\max}[j])$, and j is closest to particle i . This is fully parallel,

since the particle i will only merge with particle j if particle j is to merge with particle i . We place the merged particle at,

$$\mathbf{r}_m = \frac{m_i \mathbf{r}_i + m_j \mathbf{r}_j}{m_m}, \quad (32)$$

where $m_m = m_i + m_j$ is the mass of the merged particle. Set the velocity using the mass-weighted mean as,

$$\mathbf{u}_m = \frac{m_i \mathbf{u}_i + m_j \mathbf{u}_j}{m_m}, \quad (33)$$

similarly update other scalar properties, like, pressure, and transport velocity. Set the smoothing radius using [43],

$$h_{\text{merge}} = \left(\frac{m_m W(\mathbf{0}, 1)}{m_i W(\mathbf{r}_m - \mathbf{r}_i, h_i) + m_j W(\mathbf{r}_m - \mathbf{r}_j, h_j)} \right)^{1/d}, \quad (34)$$

where $W(\mathbf{x}, h)$ is the kernel function and d is the number of spatial dimensions. The pseudo-code for the algorithm is given in algorithm 3. Note that when merging the particles, the particle with the smaller index is the one that is retained.

After finishing the splitting, we run the merging algorithm iteratively for three times. After this, the smoothing length of all the particles is reset to the value corresponding to the average mass of the neighbors,

$$h_i = C \left(\frac{1}{\rho_0} \frac{\sum_j m_j}{N_i} \right)^{1/d}, \quad (35)$$

where C is a constant corresponding to the value of smoothing length factor used in the simulation. In our simulations we set this value to 1.2 for the quintic spline kernel.

We employ shifting after our adaptive refinement procedure. The new position \mathbf{r}'_i of the particle is given by,

$$\mathbf{r}'_i = \mathbf{r}_i + \theta \delta \mathbf{r}_i, \quad (36)$$

we correct the fluid properties by using a Taylor series approximation. Consider a fluid property φ_i the corrected value φ'_i after shifting is obtained by,

$$\varphi'_i = \varphi_i + (\nabla \varphi)_i \cdot \delta \mathbf{r}_i. \quad (37)$$

Algorithm 3 Merging of particles.

```
1: for all  $i$  which are not fixed do
2:   find neighbors of  $i$ 
3:   if  $m_i \leq m_{i,\max}$  then
4:     for  $j$  in neighbor indices do
5:        $m_{\text{merge}} \leftarrow m_i + m_j$ 
6:        $m_{\max,\min} \leftarrow \min(m_{i,\max}, m_{j,\max})$ 
7:       if  $m_{\text{merge}} < m_{\max,\min}$  &  $j$  is closest of all neighbors then
8:         store index  $j$  for merging
9: for all  $i$  of particles which are to be merged do
10:  if merge pair of  $i$  is  $j$  and merge pair of  $j$  is  $i$  and  $i < j$  then
11:    update  $\mathbf{r}_i$  with its merged pair index using eq. (32)
12:    update  $\mathbf{u}_i$  with its merged pair index using eq. (33)
13:    update  $h_i$  with its merged pair index using eq. (34)
14:  else
15:    if merge pairs match and  $i > j$  then
16:      Delete particle  $i$ 
```

Algorithm 4 summarizes the adaptive particle refinement method. First, we set the Δs of all the fluid particles in the neighborhood of a boundary to the resolution of the boundary. Next, we set Δs of all the particles which satisfy specific criteria to the highest resolution. This is useful to define solution adaptivity, where a particular flow feature is monitored, and particles exceeding specific tolerance criteria are refined to the highest resolution. After that, we run the update spacing algorithm algorithm 1 which updates the Δs of all the fluid particles. Then follows the splitting and merging procedure as described above.

The algorithms for the solution adaptivity are the same as that used in the original work of Muta and Ramachandran [1] with the difference that the properties are directly set on the fluid particles and not on the background particles. In the present work we use the vorticity to determine solution adaptivity.

3.1. Implementation in PySPH

PySPH is an open-source, Python-based, multi-CPU, and GPU framework for SPH simulations. We have used the Python based interfaces PySPH

Algorithm 4 Adaptive particle refinement procedure.

```
1: while  $t < t_{\text{final}}$  do
2:   for all fluids  $i$  do
3:     if fluid particles closest to boundary then
4:        $\Delta s_i \leftarrow \Delta s_{\text{min}}$ 
5:     if fluid particles satisfy certain criteria for solution adaptivity then
6:        $\Delta s_i \leftarrow \Delta s_{\text{min}}$ 
7:     Update the spacing of particles (algorithm 1)
8:     Split the particles (algorithm 2)
9:     for  $i = 0; i < 3; i++$  do
10:      Merge the particles (algorithm 3)
11:     for  $i = 0; i < 3; i++$  do
12:       shift the particles using eq. (36)
13:     correct the particle properties using eq. (37)
14:     update the smoothing length using eq. (35)
15:     begin the simulation using adaptive EDAC-SPH scheme (section 2)
```

provides to implement most of our adaptive algorithm. PySPH exposes Python-friendly interface to the user and using internal mechanism generates a high performance serial or parallel code based on the choice of the user. For an overview of the PySPH design, see Ramachandran et al. [49] and <https://pysph.readthedocs.io> for a detailed reference.

We use the `Tool` interface to split and merge the particles. The `Tool` interface provides a way for a user defined callback to run before or after the integration stages by overloading the `pre_stage` or `post_stage` methods, respectively. It also provides a way to run a user callback before the start of the integration step by overloading the `pre_step` method. Listing 1 shows a sample Python code used in our adaptive particle refinement algorithm. The class `AdaptiveResolution` overloads the `pre_step` method of `Tool` to run a user callback `self.run` which in turn calls other specific functions related to splitting, merging, and shifting.

Listing 1: Python code using the PySPH `Tool` interface.

```
from pysph.solver.tools import Tool

class AdaptiveResolution(Tool):
```

```

def __init__(self):
    # ...

def run(self):
    # ...
    self._add_remove_split_particles()
    if self.shifter is None:
        self.shifter = self.setup_shifting(
            self.fluid_name,
            [self.fluid_array],
            self.nnps, self.dim,
            rho0=self.rho0, iters=3
        )
    self.shifter.update()
    self.shifter.evaluate()

def pre_step(self, solver=None):
    # ...
    self.count += 1
    if self._count % self.freq == 0:
        self.run()

```

These functionalities enable one to write the code without having to pay much attention to the low-level high-performance complexities of implementing on different platforms like multi-core CPUs, or GPUs. The respective splitting and merging algorithms are all implemented in pure Python. For complete details of our implementation one can see the source code provided in https://gitlab.com/pypr/asph_motion.

In section 5.4 we solve a case with a stationary cylinder and another with a moving square to demonstrate that we do not require the background particles. In section 5.6 we demonstrate the parallel performance of our algorithms by solving a problem and studying the speedup obtained as we increase the number of threads.

4. Source files description

The algorithms mentioned in the manuscript are primarily contained in the following files located in the `code/` directory: `edac.py`, `adapt.py`, `adaptv.py`, and `no_bg.py`. The `hybrid_inlet_outlet.py` contains the code which implements

the no-reflection boundary conditions of [62] and manages the inlet/outlet particles.

We use `automan` [50] Python package to automate all of our results. The file `automate.py` contains the code to generate all the results used in this paper. See `README.md` for more details regarding the individual run time of the problems in `automate.py`. The following files in the `code/` directory contain the test problems used in the manuscript:

- `fpc_auto.py`: Flow past a stationary cylinder.
- `moving_square.py`: Flow past a moving square (SPHERIC test 6).
- `ellipse_plunging.py`: Flow past a plunging ellipse at $Re = 500$.
- `ellipse_tranlation.py`: Flow past a translating ellipse at $Re = 500$.
- `fpc_bao_static.py`: Flow past two stationary cylinders at $Re = 100$.
- `fpc_bao_oscillation_1cylinder.py`: Flow past single oscillating cylinder at $Re = 100$.
- `airfoil_stationary_naca.py`: Flow past a stationary NACA5515 airfoil.
- `s_shape.py`: Flow past a rotating S-shape at $Re = 2000$.
- `sun_airfoil08_aoa4.py`: Flow past a NACA0008 airfoil at 4° angle of attack and $Re = 2000$.
- `sun_airfoil12_aoa6.py`: Flow past a NACA0012 airfoil at 6° angle of attack and $Re = 6000$.
- `performance.py`: Code to measure the parallel performance of the algorithms.

5. Results and Discussion

In this section we demonstrate practical applications of the adaptive smoothed particle hydrodynamics method for selected problems in two dimensions. The problems considered are fairly challenging to solve without the adaptive refinement. We consider moving and stationary geometries specifically focusing on the following problems:

1. flow around two stationary cylinders in a side-by-side configuration with different gap spacings;
2. flow over airfoils with different NACA profile at different Reynolds numbers and angles of attack;
3. flow around a moving square at different Reynolds numbers; and,
4. flow around a single oscillating cylinder with different oscillating frequencies.

5.1. Flow around two stationary cylinders in a side-by-side configuration

We study the flow around two stationary cylinders in a side-by-side configuration at $Re = 100$. The flow produces distinct wake patterns at different gap spacing between the cylinders. This problem is studied first by Kang [64] and further used as a validation test case by Bao et al. [65] but do not have SPH related studies. The diameter D of each of the cylinders is $1m$. The dimensions of the computational domain are based on D , and the schematic diagram of the computational domain is shown in fig. 2. For each inlet, outlet, and wall, we use 10 layers of particles to get full kernel support. Three different cases of center-to-center cylinder spacing $S = 1.2D, 1.5D$ and $4D$ are considered for simulations. A constant velocity is prescribed at the inlet, $U_\infty = 1m/s$, and the kinematic viscosity ν is given by $U_\infty D/Re$. Other geometric and numerical parameters are provided in Table 1. For all the

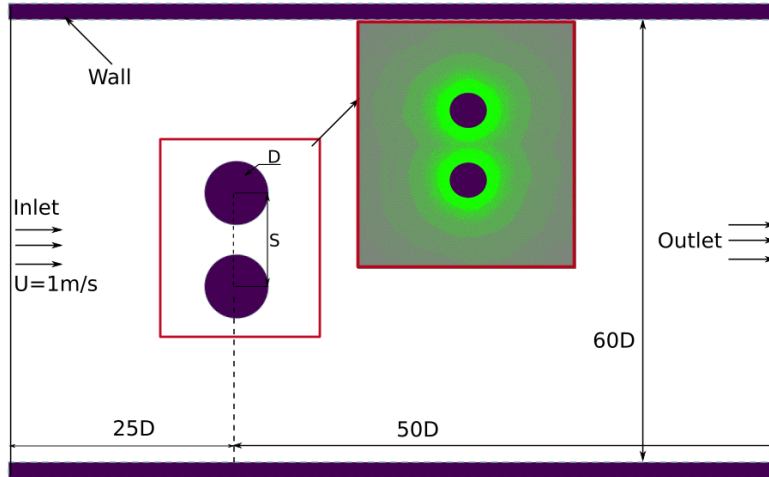


Figure 2: Schematic of the computational domain for the simulation of flow past two cylinders in a side-by-side arrangement.

Table 1: Simulation parameters for the problem described in 5.1.

Parameter	Value	Parameter	Value
D	$1m$	U_∞	$1m/s$
S	$D(1.2 - 4.0)m$	ρ	$1000kg/m^3$
ν	$U_\infty D/Re$	ω	0

cases, we deploy particles in the range of $75k$ to $88k$ on a $75\text{ m} \times 60\text{ m}$ domain. The maximum spacing of fluid particles is $D/\Delta x_{\max} = 2$ and the minimum resolution of the fluid particles, which also matches the resolution of the boundary, is $D/\Delta x_{\min} = 100$; the ratio of which is 50 times smaller. Without an adaptive resolution, the problem would need 45 million particles to simulate at such accuracy using the minimum resolution.

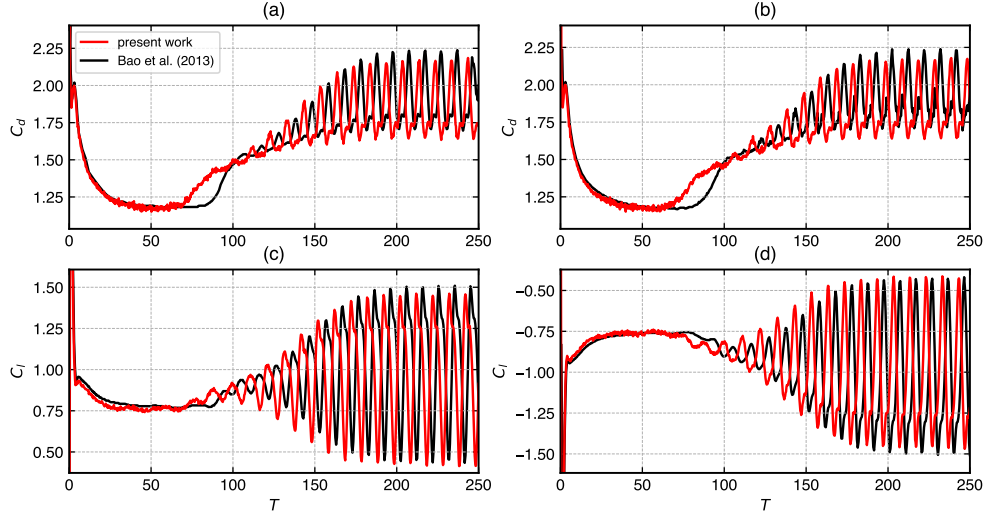


Figure 3: Time history of the drag and lift force coefficients for two stationary cylinders in a cross-flow at $Re = 100$. Comparison of adaptive EDAC-SPH results with [65] for gap spacing ratio of $S = 1.2D$. (a) C_d upper cylinder, (b) C_d lower cylinder, (c) C_l upper cylinder, (d) C_l lower cylinder.

We are able to observe the three kinds of vortex shedding wake patterns that occur for each configuration. The wake patterns are (i) single bluff body at $S = 1.2D$, (ii) a random flip-flopping gap at $S = 1.5D$, and (iii) anti-phase synchronized wake at $S = 4.0D$. Time evolution of the simulated results of total drag and lift force coefficients are presented in figs. 3 to 5. The

simulations took a fairly long wall-clock time for 250 seconds of simulation time, each case requiring an average wall-clock time of 40 hours on a server with 16 cores and 32 threads for the adopted resolution.

Figure 3 shows the comparison of time history of the coefficients of total drag and lift for spacing $S = 1.2D$ up to $T = U_\infty t/D = 250$. The figure illustrates the force characteristics of a single bluff body type with entirely suppressed gap flow observed at ($S = 1.2D$).

Our results show a phase difference which may be caused by the differences in the nature of the solvers, time-stepping used, and boundary conditions. The results are in good agreement with the reference data of [65]. The trend, as well as the magnitude of the curves, is matching well.

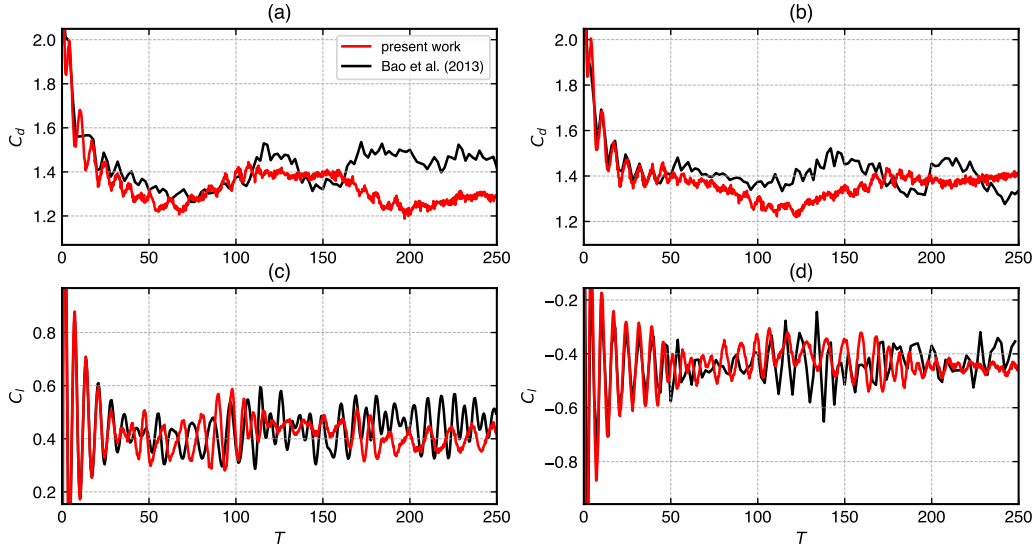


Figure 4: Time history of the drag and lift force coefficients for two stationary cylinders in a cross-flow at $Re = 100$. Comparison of adaptive EDAC-SPH results with [65] for gap spacing ratio of $S = 1.5D$. (a) C_d upper cylinder, (b) C_d lower cylinder, (c) C_l upper cylinder, (d) C_l lower cylinder.

Figure 4 shows the force characteristics for the spacing $S = 1.5D$. The flow is complicated and belong to a randomly flip-flopping flow for which the wake pattern looks irregular [65]. Our results compare very well at the beginning up to around 75 seconds of the flow. The results show some discrepancy in the C_d afterward but stay in the trend, matching the amplitude and frequency.

The C_l results match better than the C_d in all the cases for both the top as well as bottom cylinders.

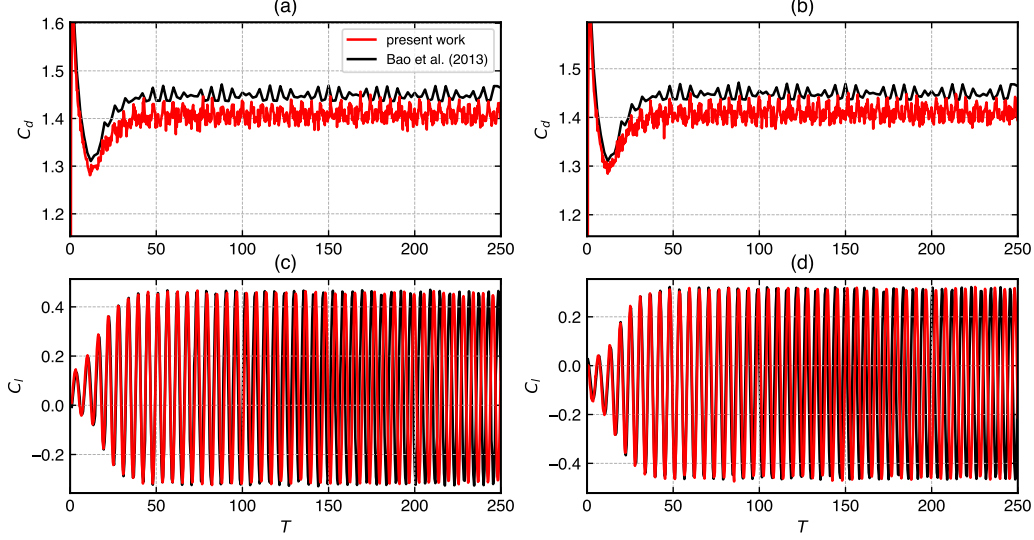


Figure 5: Time history of the drag and lift force coefficients for two stationary cylinders in a cross-flow at $Re = 100$. Comparison of results of the present model with [65] for gap spacing ratio of $S = 4.0D$. (a) C_d upper cylinder, (b) C_d lower cylinder, (c) C_l upper cylinder, (d) C_l lower cylinder.

Figure 5 displays the comparison of results for the coefficients drag and lift force at spacing $S = 4.0D$. The results are matching well with the C_d of the reference data in fig. 5 (a) and fig. 5 (b) of the upper and lower cylinders with differences less than 5 percent. The results of C_l are in a very good agreement as shown in fig. 5 (c) and fig. 5 (d) for both the cylinders. The force characteristics of the flow at this gap between the cylinders is anti-phase synchronized where the vortex is shed behind each cylinder independently and symmetrical to the centerline.

Figure 6 exhibits the vorticity distribution corresponding to the three spacing ratios. The results indicate that the flow characteristics and wake structure explained in Figs. 3 to 5 are justified. The flow structure strongly depends on the spacing gap for the given Reynolds number. A suppressed flow, seemingly a single bluff-body wake pattern is shown by the smallest spacing of $S = 1.2D$ in fig. 6a. In fig. 6b the gap flow flip-flops for $S = 1.5D$ and seems irregular. The wake pattern changes to a synchronized flow as the spacing increases.

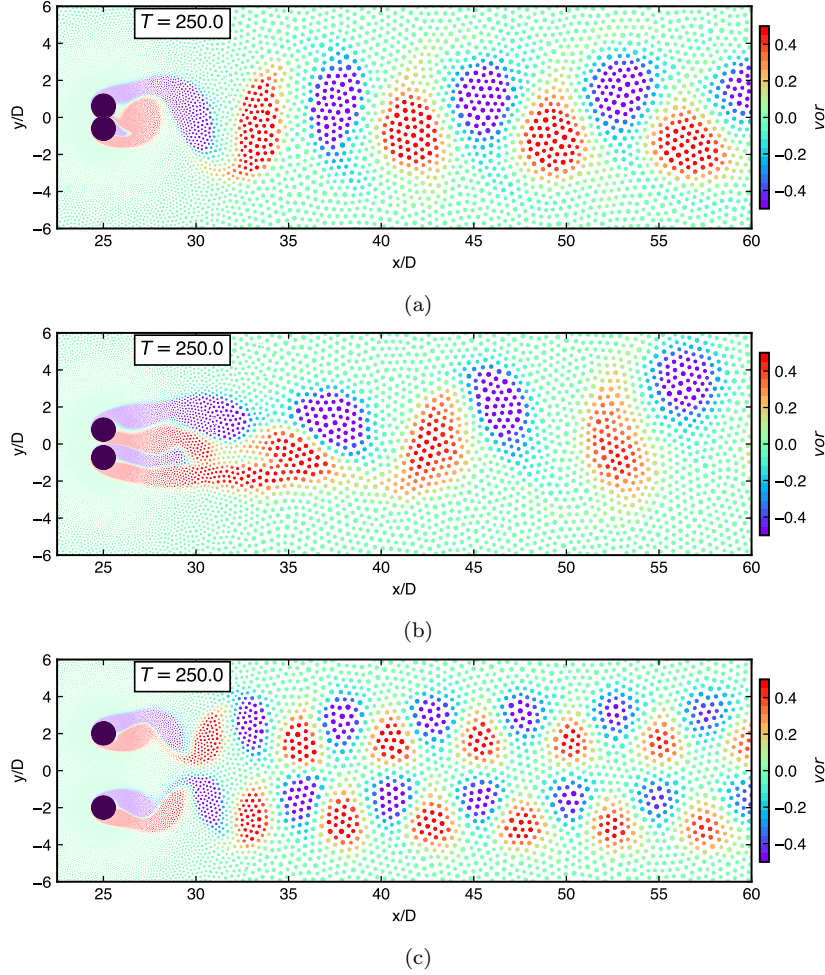


Figure 6: Vorticity distribution corresponding to flow past two stationary cylinders in a side-by-side arrangement at $Re = 100$ with the gap spacing ratio of, (a) $S = 1.2D$; (b) $S = 1.5D$; (c) $S = 4.0D$. The size of the points is proportional to the mass of the particles.

As shown in fig. 6c, the instantaneous wake is anti-phase synchronized; the vortex shedding occurs completely behind each cylinder which is symmetric with the wake centerline.

The behaviour of the flows around two stationary cylinders and a single oscillating cylinder, or both is helpful to understand the mechanism of flow around two or more oscillating cylinders. The present SPH model is able to simulate and accurately identify the wake characteristics of the flow. The

force quantities are in general in good agreement with the results available in the literature. This accuracy is achieved with a proper particle resolution using a reduced total number of particles.

5.2. Flow over airfoils with NACA profile

Flow around airfoil present difficulties to conduct high accuracy SPH simulation. It can be more difficult when it is thinner, particle distribution is irregular, or if it is moving. It is further challenging in complex motion applications like in a rotational motion, elliptic motion, and motions which combine heaving, oscillation, and pitching. One of the first applications of SPH to model flow around an airfoil was conducted by Shadloo et al. [66] and [67] in which they have shown a comparative study between the weakly compressible and incompressible SPH methods. However, their results have shown poor accuracy even when employing large number of particles at moderate Reynolds number. With the help of multi-resolution and particle shifting technique, Sun et al. [68] indicated an improved success of airfoil SPH simulation for Reynolds number up to 10,000. Huang et al. [20] illustrated an improved simulation of viscous fluid flow around airfoils using SPH scheme possessing iterative particle shifting technology (IPST) and which does not use kernel gradients. The numerical study of airfoil motion is important for application like in unmanned aerial vehicles (UAVs) for thrust generation and in vertical axis wind turbines (VAWTs) for power optimization.

We discuss three stationary airfoil cases: (i) NACA5515 airfoil at $\alpha = 5^\circ$ and $Re = 420$, (ii) NACA0008 at $\alpha = 4^\circ$ and $Re = 2000$, (iii) NACA0008 at $\alpha = 4^\circ$ and $Re = 6000$. The computational domain is $[-3L, 7L] \times [-3L, 3L]$, where $L = c = 1$ m is the characteristic length (chord) with center at the airfoil midpoint. The algorithm of Negi and Ramachandran [63] is used for packing the airfoils.

5.2.1. NACA5515 airfoil at $\alpha = 5^\circ$ and $Re = 420$

Figure 7 depicts boundary points of NACA5515 marked in yellow color and inner particles of the solid in violet. The particles on surface of the airfoil (boundary points) are identified by computing divergence of the position vector. All the surface points are identified correctly when the computed value is lower than $d - 0.625$, d is the dimension. The airfoil particles are packed with the smallest spacing, $L/\Delta x_{\min} = 80$, which is equal to the

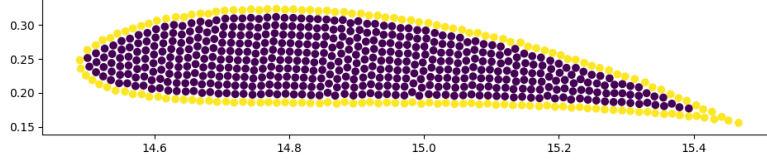


Figure 7: Airfoil with NACA5515 profile at 5° angle of attack, yellow color indicates the surface particles. Particles are packed at a resolution $L/\Delta x = 80$ with the algorithm described in Negi and Ramachandran [63].

minimum resolution of fluid particles for mapping. We have simulated for $T = 12$ and compared the results with [20].

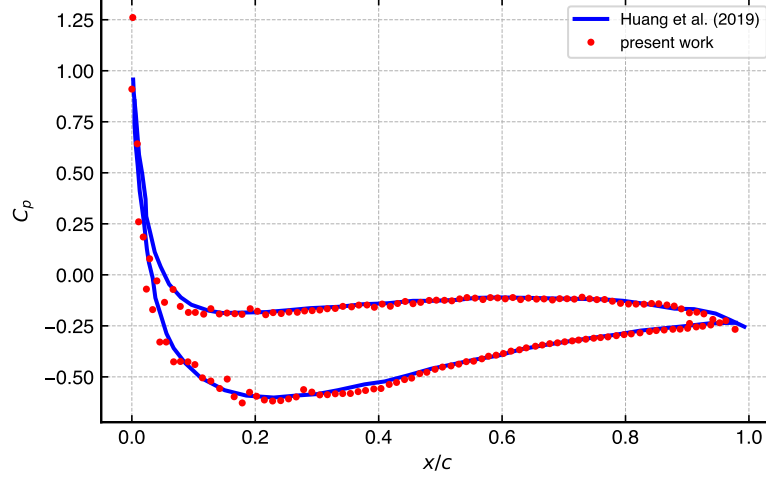


Figure 8: Comparison with [20] of pressure coefficient C_p on the surface of NACA5515 airfoil at $T = 12$, with $\alpha = 5^\circ$, and $Re = 420$.

Figure 8 shows the coefficient of pressure C_p on the surface of an airfoil with the NACA5515 profile. The airfoil is at an angle of attack $\alpha = 5^\circ$, $Re = 420$ and uses particle spacing $L/\Delta x_{\min} = 80$. The simulated result of the present model agrees very well with [20]. Based on the information provided in [20], about $360k$ particles are employed to produce their result. However, our solution require around $40k$ particles which could be considered as a massive gain due to the adaptive resolution.

5.2.2. NACA0008 airfoil at $\alpha = 4^\circ$, $Re = 2000$ and $Re = 6000$

The airfoil in NACA0008 profile has very thin cross-section which makes it a challenging problem for numerical methods. This section discusses the flow around the airfoil at an angle of attack $\alpha = 4^\circ$. We simulate the problem for two different Reynolds numbers which are 2000 and 6000. The total drag and lift coefficient of the simulated results are compared with Diffused Vortex Hydrodynamics (DVH) method of Rossi et al. [69], and SPH method of Sun et al. [68].

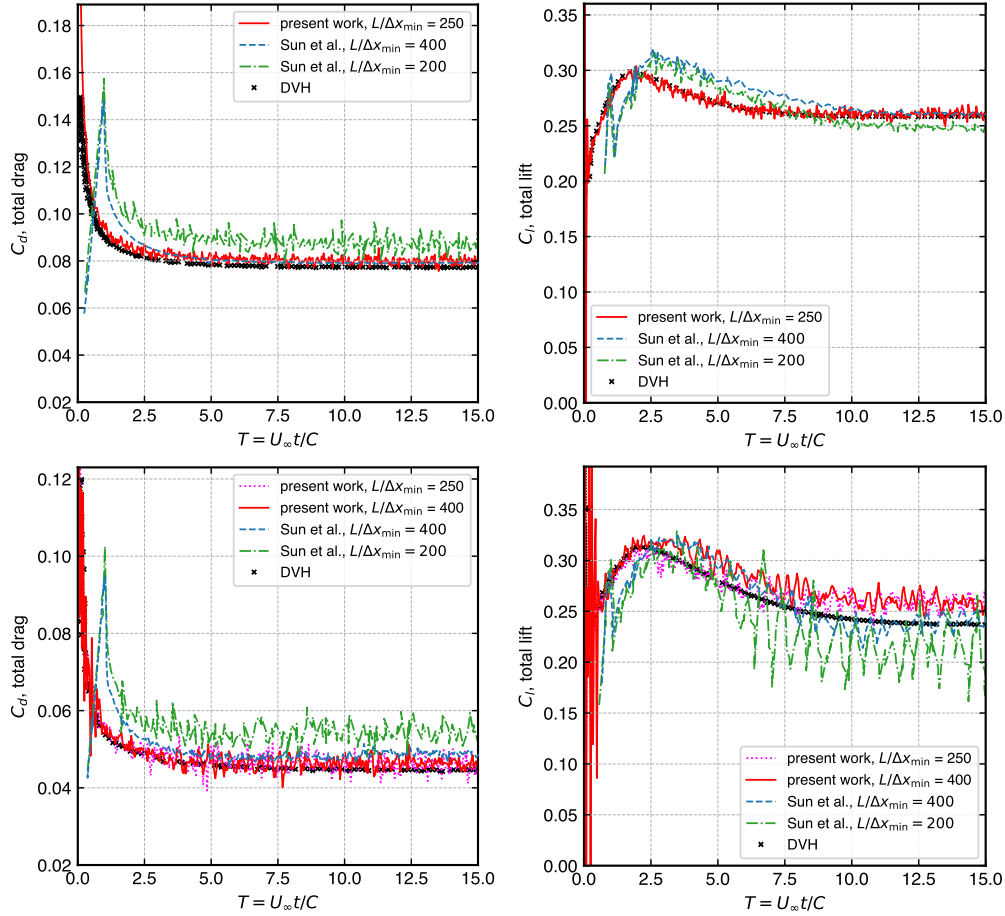


Figure 9: Flow over NACA0008 airfoil at $\alpha = 4^\circ$ at $Re = 2000$ (upper) and $Re = 6000$ (lower). Evolution of the drag (left) and lift (right) force coefficients. Comparison of the results with DVH [69] and Sun et al. [68].

Figure 9 illustrates the evolution of force coefficients drag (left) and lift

(right). We simulate for $T = 15$ using $L/\Delta x_{\min} = 250$ for $Re = 2000$ (top) and $L/\Delta x_{\min} = 250, 400$ for $Re = 6000$ (bottom). At this resolution our simulations show very good comparison with DVH [69] and have improved results compared with [68]. The trend of the curve is captured very well except some oscillations that can be minimized by increasing the resolution. Sun et al.’s result of comparable resolution has higher noise and misses some features of the curve. Also, the number of particles (from Sun et al.’s Fig. 3) is more than $250k$ particles for $L/\Delta x_{\min} = 400$, whereas our adaptive EDAC-SPH simulation employs around $77k$ particles.

Table 2 shows the number of particles used in the simulation for two different Reynolds numbers. The number of particles is about 3.25 times less than [68].

Method	$Re = 2000$	$Re = 6000$	$L/\Delta x_{\min}$
Sun et al. [68]	$250k$	$250k$	400
Adaptive EDAC-SPH	$76.5k$	$76.5k$	250
Adaptive EDAC-SPH (solution adaptivity)	—	$260k$	250

Table 2: Flow over NACA0008 airfoil at $\alpha = 4^\circ$. Comparison between the approximate number of particles used in [68] and adaptive EDAC-SPH.

We ran the $Re = 6000$ case with and without solution adaptivity, where the vorticity particles exceeding 5% of the maximum vorticity in the domain are refined to the highest resolution. The number of particles increases to $260k$. There is no significant difference in the lift or drag coefficient of the airfoil between the solution adaptive and without the solution adaptive case since the solid bodies are initially discretized at the highest resolution. Our non-solution adaptivity case took about 18 hrs, whereas the solution adaptivity case took about 41 hrs.

In fig. 10, we display the vorticity field around NACA0008 airfoil at an angle of attack $\alpha = 4^\circ$. The top figure is simulated without solution adaptivity at $Re = 2000$, and the bottom is simulated using solution adaptivity at $Re = 6000$. Due to the small angle of attack, the viscous flow remains attached to the surface where a steady regime has reached immediately. The selected airfoil configuration has practical application in micro-aerial vehicles (MAVs) for the Reynolds numbers in the given range [69].

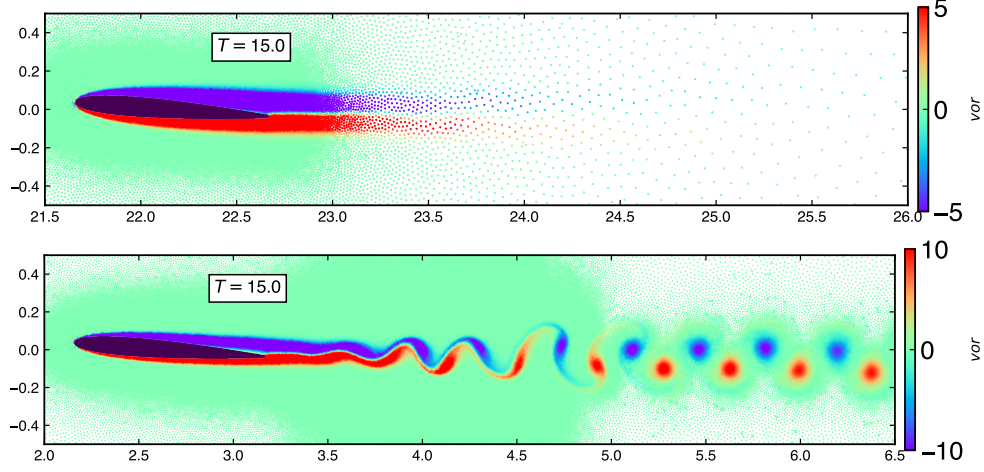


Figure 10: Vorticity field around NACA0008 airfoil at of at $\alpha = 4^\circ$. Simulated without solution adaptivity $Re = 2000$ (top), and using solution adaptivity at $Re = 6000$ (bottom).

5.3. Flow around a moving square

The flow around a moving square represents a simple geometry but a flow situation that can be very complex due to the sharp edges. The problem consists of a square geometry moving through a stationary fluid kept inside a rectangular box. The test can generate intense unsteady vorticity and has been a challenging test case for SPH solvers. This simulation is part of a validation test suite compiled by the SPH rEsearch and engineeRing International Community (SPHERIC) [70]. The benchmark results of this test case are simulated using Finite Difference Navier-Stokes (FDNS) solver by [71]. In SPH [43], and [72] studied this problem. We study the time histories for the drag force coefficients (pressure, viscous or total) and the generation and diffusion of vorticity.

The geometric configuration is shown in fig. 11a at time $t = 0$. The body motion in time is shown in fig. 11b. The domain size is $L_y \times L_x = 5 \text{ m} \times 10 \text{ m}$, with the square obstacle having a length of 1m. The square motion is prescribed with a smooth acceleration in the x -axis starting from rest until it reaches a steady maximum velocity $U_{\text{square}} = 1.0 \text{ m/s}$. The boundary conditions are no-slip and no-reflection on all walls of the rectangular domain and slip velocity on the solid square. The simulation is conducted for a Reynolds number of 100 with no gravity force and zero initial pressure field for the viscous incompressible Newtonian fluid of density 1 kg m^{-3} .

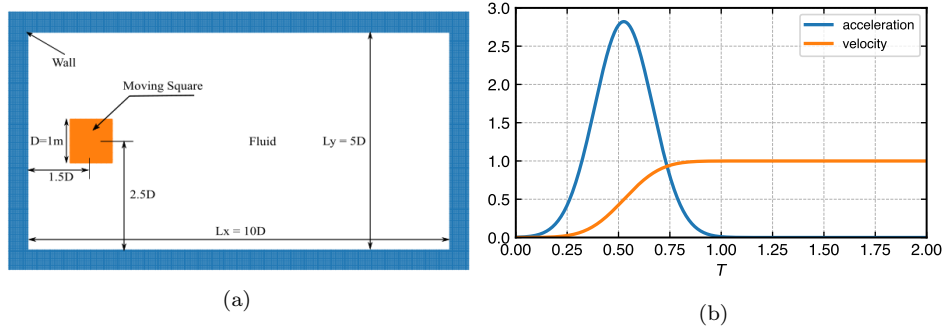


Figure 11: Flow around a moving square, (a) Moving square test case geometry, (b) the body motion in time.

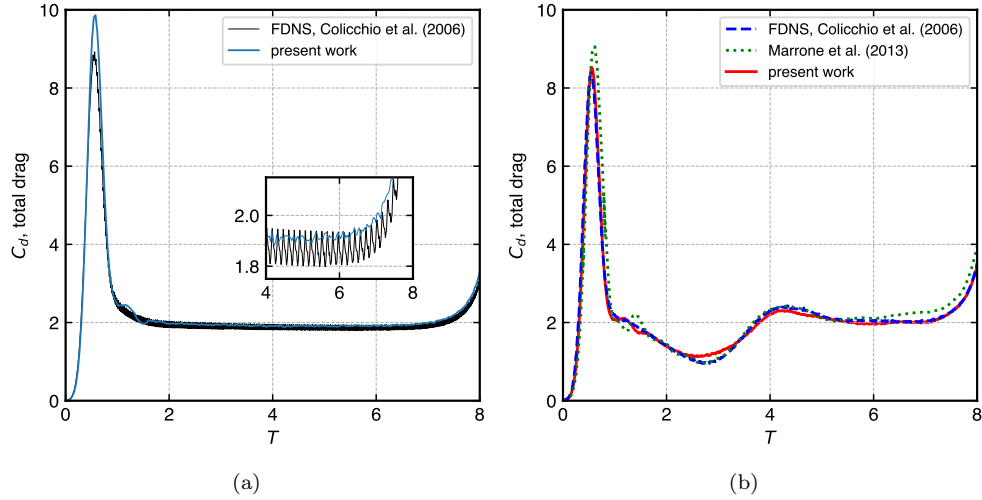


Figure 12: Comparison of the total drag coefficient for a square cylinder at (a) $Re = 100$ and (b) $Re = 600$. Simulated results of adaptive EDAC-SPH are compared with FDNS solver [71] and Marrone et al. [72].

In fig. 12, we show the time evolution of the drag coefficient of a moving square at (a) $Re = 100$ using $D/\Delta x_{\min} = 80$ and (b) at a slightly higher Re of 600 using $D/\Delta x_{\min} = 200$. Simulated results obtained from the present method are compared with the results of the FDNS solver [71] and Marrone et al. [72]. The comparison shows, especially with FDNS, very good agreement with all the necessary features.

The simulation requires $44k$ fluid particles using adaptive resolution for the converged solution. The initial spacing of particles on the domain is $\Delta x_{\max} = 0.04$; the smallest spacing is $\Delta x_{\min} = 0.0125$ near the obstacle. The solid particles are packed using the minimum resolution to create a mapping in the fluid-solid interface. If the Δx_{\min} was used in the entire domain, $D/\Delta x_{\min}$ would be 80 which produces $320k$ as the total number of particles. However, with an adaptive particle resolution, we have used only $44k$ particles to produce accurate results. This substantially reduces the number of particles by 7.273 times when compared with Marrone et al., [72] and by four times when compared with the results by [71].

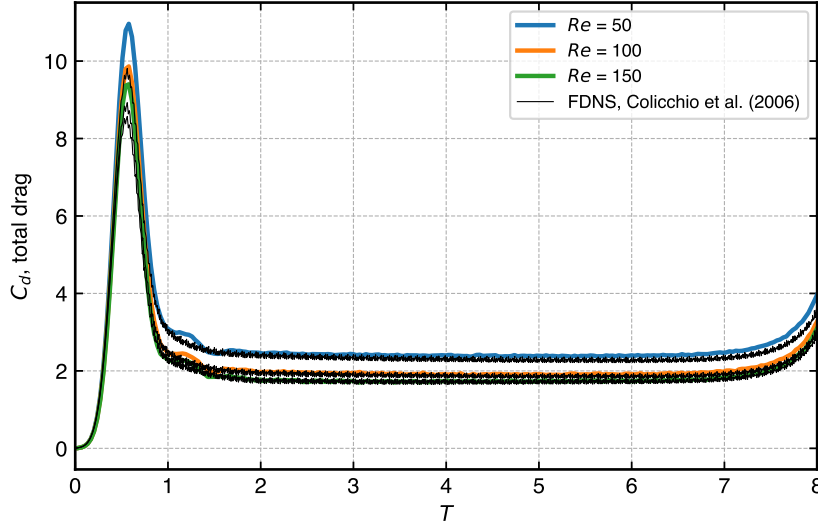


Figure 13: Comparison of results against the results of Colicchio et al. [71], with varying Reynolds number, for flow around a moving square.

Figure 13 shows the variation of drag coefficient for flow around a moving square at different Reynolds numbers. The comparison is made for three Reynolds numbers of 50, 100, and 150. The results of the adaptive EDAC-

SPH are in good agreement with [71] results. However, due to numerical reasons [71] show the small amplitude and high-frequency oscillations which are avoided in our case.

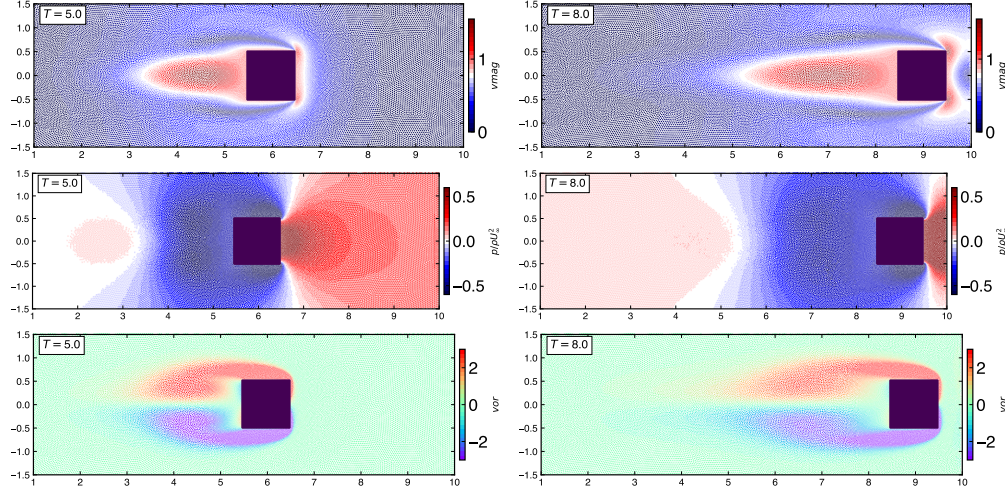


Figure 14: Particle distribution of moving square problem at $T = 5$ (left), and $T = 8$ (right) for $Re = 100$ showing: velocity magnitude (top), pressure (middle), and vorticity (bottom). The lowest resolution used is $D/\Delta x_{\max} = 25$ and the highest resolution used is $D/\Delta x_{\min} = 80$.

Figure 14 show the particle distribution with color indicating pressure, vorticity and velocity magnitude taken at $T = 5$ and $T = 8$. The qualitative observations illustrate the generation, diffusion, and convection of the unsteady vorticity proving the capability of the adaptive EDAC-SPH scheme.

5.4. Removal of background particles

Muta and Ramachandran [1] used a collection of particles called “background” particles to define the particle spacing Δs and reference mass. But in this work, we show that the background particles are not necessary to set this reference mass. Updating the reference mass on the particles themselves produces results closely matching those produced by the original algorithm using background particles. This reduces memory usage by removing background particles’s storage, and a small reduction in the computational time. We perform two simulations to establish the no background particle approach. We first consider the flow past a circular cylinder at $Re = 1000$, the simulation parameters and domain sizes are the same as defined in [1]. Furthermore, we

compare the results with the established vortex method results [73, 74]. We then consider the flow past a moving square in a box at $Re = 150$. Refer to section 5.3 for the simulation parameters. We compare the results to the incompressible FDNS simulation results [71]. In this case, the geometry is moving. In addition, we use solution adaptivity to refine the particles to the lowest resolution where the vorticity exceeds 5% of the maximum vorticity in the simulation.

Figure 15a shows the time history of the drag coefficient of the flow past cylinder problem without solution adaptivity. The results of adaptive EDAC-SPH are computed with and without use of background particles, and both results match very well with the reference data from vortex method simulations. Figure 15b shows the time history of the drag coefficient of the moving square problem using solution adaptivity. This further confirms a good match when not using the background particles. Figure 16a we show the distribution of the spacing Δs without using background particles and in fig. 16b we show the vorticity distribution. It can be seen that the regions satisfying the solution adaptivity criteria are refined to the highest resolution, and the particles closest to the solid square particles are refined to the highest level.

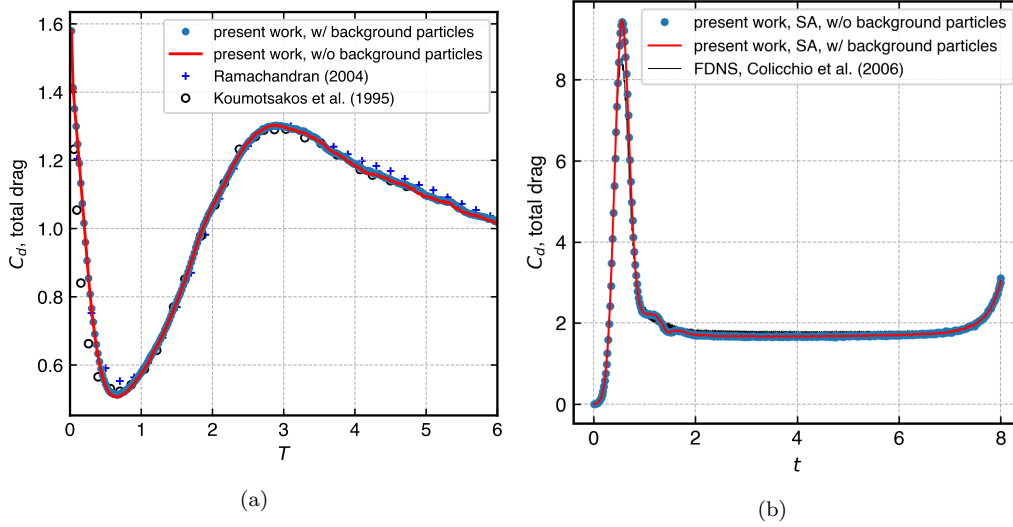


Figure 15: (a) Comparison of the drag coefficient vs time with and without the use of background particles to that of the vortex method results[73, 74]. (b) Time history of the drag coefficient of a moving square simulated using solution adaptivity (SA) at $Re = 150$ compared against FDNS results[71].

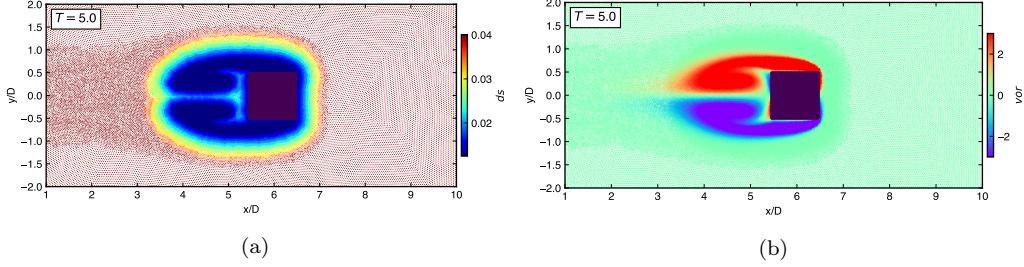


Figure 16: (a) Δs distribution (b) Vorticity distribution for the flow past a moving square at $Re = 150$, the highest resolution $D/\Delta x_{\min}$ is 80 and the lowest resolution $D/\Delta x_{\max}$ is 25, and a C_r spacing ratio of 1.12 is used.

5.5. Flow around an oscillating single cylinder

The numerical examination of flow around an oscillating single cylinder is helpful for the simulation and deeper analysis of two or more oscillating cylinders. The study of flow over a cylinder is important for the study and design of flow over a car, flow over aircraft, flow over airfoil blades, or flow over a pillar for the design of bridges [64, 65, 75, 76, 77].

Bao et al., [65] classify the flow around the oscillatory motion of cylinders into lock-on and unlock-on states which are also characteristic of two cylinder flows. The classification depends on the shedding and oscillating frequencies for which the transition occurs around a frequency ratio of one.

We analyze the oscillatory motion of a single cylinder subject to cross-flow at $Re = 100$. The sinusoidal motion of the cylinder is defined by $Y = A \sin(\omega t)$, where A is the amplitude, $\omega = 2\pi f$ the angular velocity, and f the frequency of oscillation. Two amplitudes of oscillation (low and high) and frequency ratio (f_R) ranging from low to high are chosen for the simulation. Here $f_R = f/f_0$, where f_0 is a natural vortex shedding which is 0.165 for a single cylinder oscillating at $Re = 100$. The values are $A = (0.25, 1.25)D$ and $f = (0.5, 1.5)f_0$.

Figure 17 shows the time history of the fluctuating lift coefficient for four combinations of amplitude and oscillation frequency. The range includes lock-on and unlock-on states. In fig. 17a $(A/D, f_R) = (0.25, 0.5)$, the simulated results initially show faster transition and match with [65] capturing the peak-to-peak amplitude and all trends. In fig. 17b $(A/D, f_R) = (0.25, 1.1)$, our simulation depicts pure sinusoidal oscillation from the beginning, matching

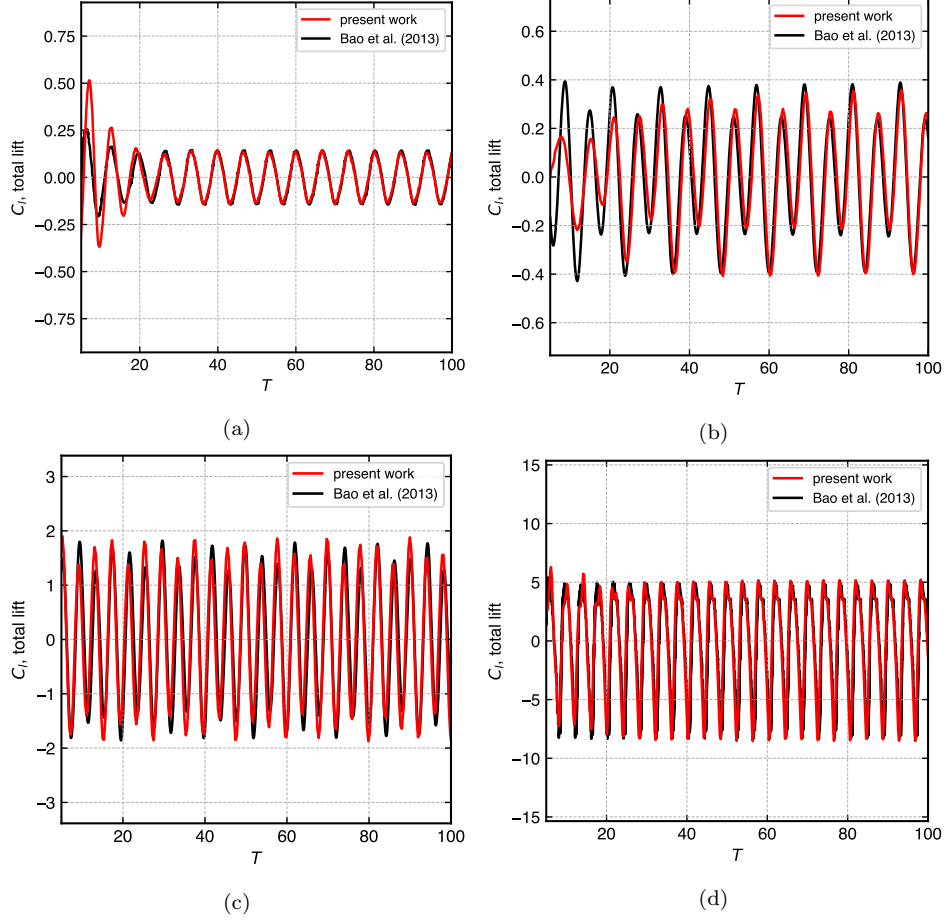


Figure 17: Time history of the lift coefficient for a single cylinder oscillating at $Re = 100$ with different oscillating frequencies, Lock-on state: (a) $(A/D, f_R) = (0.25, 0.9)$; Unlock-on state: (b) $(A/D, f_R) = (0.25, 0.5)$, (c) $(A/D, f_R) = (0.25, 1.5)$, (d) $(A/D, f_R) = (1.25, 1.5)$, compared with the results of Bao et al. [65].

very well for $t \geq 80$ seconds. The fluctuating lift coefficient beats with a stronger magnitude for higher oscillating frequencies. Figure 17c $(A/D, f_R) = (0.25, 1.5)$, takes a combination of the smallest amplitude ratio with the highest value of the oscillating frequency, the results match very well from the beginning. In fig. 17d $(A/D, f_R) = (1.25, 1.5)$, both parameters of the amplitude and oscillating frequency are on the higher side. The results of this simulation capture all the trends and peaks of the lift coefficients fluctuation and are in good comparison with the reference data.

5.6. Performance analysis

In this section, we discuss the parallel performance of the adaptive EDAC-SPH implemented using the framework of PySPH. To show that our adaptive algorithm is fully parallel, we run the moving square test case with the highest resolution of $\Delta x_{\min} = 0.0075$ and the lowest resolution of $\Delta x_{\max} = 0.2$, giving us 57k particles. As opposed to the gradual start in the moving square problem described in section 5.3 we move the solid with a uniform velocity of 1 ms^{-1} . We proceed to test this problem on a 6-Core Intel Core i7 CPU. We compare the time taken to run 1000 time-steps on a serial single-core single-thread execution with a parallel (OpenMP) execution on the multi-core CPU with 4-threads and 6-threads.

Component	1-thread	4-threads	6-threads
splitting & merging	24.74 s	7.91 s	6.64 s
removing & adding particles	0.63 s	0.61 s	0.70 s
EDAC scheme	260.77 s	78.44 s	64.38 s

Table 3: The time break-up for running 1000 time-steps of the moving square problem executed on a serial single-thread, and parallel 4-threads and 6-threads on a 6-core CPU.

Table 3 shows the time taken by various algorithms described in this manuscript along with the time taken by the adaptive EDAC-SPH scheme. The splitting and merging component constitutes the Update Spacing algorithm 1, splitting algorithm 2, and merging algorithm 3; the removing and adding of particles constitutes for the time taken by the removal of the merged particles’ indices from the data structure, and addition of new particles to the data structure; the EDAC scheme constitutes the overall time taken by the SPH formulation.

Table 3 shows that the multi-thread implementation scales well in parallel with a scale-up of 3.13x on 4-threads and 3.73x on 6-threads. The time taken for removing and adding particles to the data structure constitutes less than 2.5% of the adaptive algorithm and this process is serial in execution. The present scheme again scales well with an increase in number of threads. The scale-up is 3.32x on 4-threads and 4.05x on 6-threads. The parallel execution of the adaptive algorithm constitutes 10–11% of the adaptive EDAC-SPH scheme.

The results of this section validate our formulation with the existing numerical simulations.

6. Complex motion demonstration

Simulation of fluid flow around moving solid bodies is challenging and even more challenging in complex motion scenarios such as the rotation of a complex geometry and motions that combine pitching and translating. The adopted adaptive EDAC-SPH method automatically refines the particles around solid bodies performing any type of motion. Applications in complex moving cases are demonstrated in this section. We consider the following examples for the demonstration:

1. translating and pitching ellipse;
2. plunging ellipse with elliptical motion trajectory; and,
3. rotating S shape.

An elliptic solid body and an S shape are used to illustrate the various motions. The ellipse has a characteristic length of 1 m and axis ratio 0.4. All the test cases use boundary conditions of the moving square problem discussed in section 5.3 for a stationary fluid.

6.1. Translating and pitching ellipse

The acceleration of the center of mass of the ellipse, $a_{\text{cm}}(t)$, and the instantaneous pitch angle with respect to the horizontal, $\theta(t)$, are given by,

$$a_{\text{cm}}(t) = b_0 \exp\left(\frac{-(t - b_1)^2}{2c^2}\right) + d, \quad (38)$$

$$\theta(t) = \theta_0 \sin(\omega t + \psi) \quad (39)$$

where $b_0 = 2.8209512$, $b_1 = 0.525652151$, $c = 0.14142151$, $d = -2.55580905e - 08$, and the pitch amplitude $\theta_0 = 10^\circ$ are the constants.

We simulate the translating and pitching ellipse in a rectangular domain of size $L_y \times L_x = 5c \times 10c$ at a Reynolds number of 550. The ellipse is started with a smooth acceleration in the x -axis starting from rest until it reaches a steady maximum velocity of 1 m s^{-1} . The schematic of the domain is shown in fig. 18. The wall boundary condition is the same as that used in the moving square problem of section 5.3. Figure 19 shows the vorticity distribution around the ellipse at different times. The top figure is at $T = 1.3$, where the ellipse is 0° from the horizontal. The middle figure is at $T = 4.5$, where the ellipse is at 10° from the horizontal and the bottom figure is at the final time of $T = 8$.

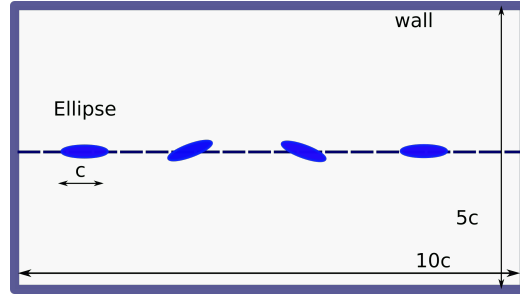


Figure 18: Translating pitching motion of an ellipse at four different times.

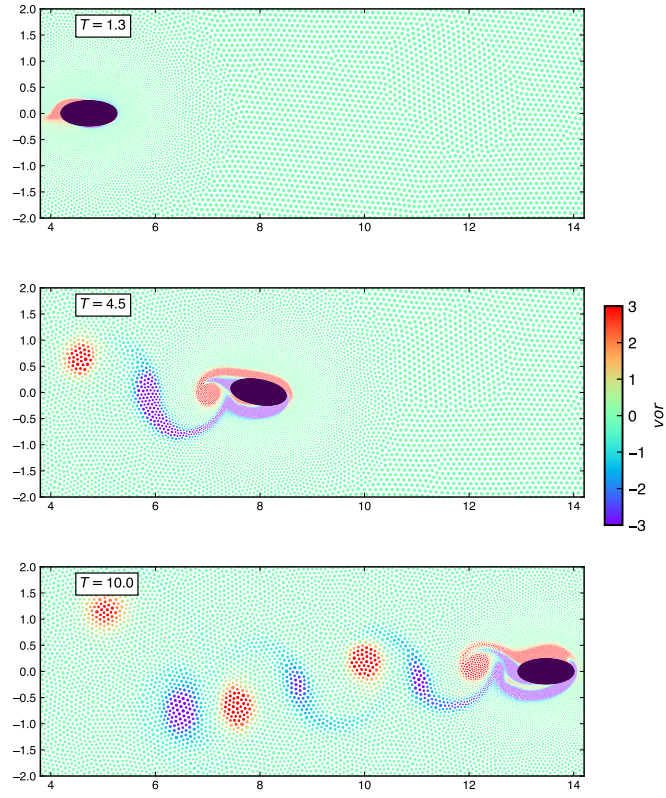


Figure 19: Vorticity distribution around a translating and pitching ellipse at three different times with the point size corresponding to the mass of the particle.

6.2. *Plunging ellipse with elliptical motion trajectory*

Kinematics of a flapping motion describes a vertical translation (heaving), a horizontal oscillation, and pitching rotation. The amalgamation of these motions constructs an elliptical trajectory (path) of the pitching ellipse. This kind of kinematics is seen in the flying birds, aquatic animals, and has potential applications in high-efficiency Micro Air Vehicles (MAVs), and other energy harvesting vertical axis wind turbine (VAWT) designs [78, 79, 80, 81]. The pitching orientation and angle of attack can also vary according to the type of motion undertaken for high-level performance. The schematic diagram of ellipse motion is shown in 20. The motion equations for the vertical plunge,

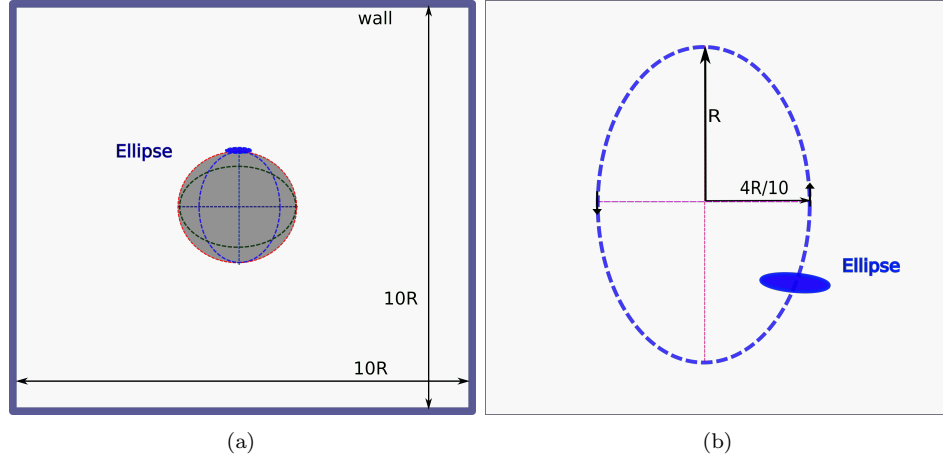


Figure 20: Schematic diagram of the ellipse in plunging motion: (a) Domain size and boundary condition, (b) Enlarged view of the rotating area.

($h(t)$), and the horizontal sinusoidal motion, $w(t)$, of the ellipse are defined by,

$$h(t) = h_0 \cos(\omega t), \quad w(t) = bh_0 \sin(\omega t), \quad (40)$$

where $h_0 = 2$, $\omega = 2\pi/5$ is the angular velocity, and $b = 0.5$ is a factor relating a horizontal motion with the vertical counterpart.

Figure 21 shows the vorticity plots of a plunging ellipse undergoing the mixed vertical-horizontal oscillatory motions forming an elliptical trajectory. The motion of the solid ellipse is described using the equations in 40, of a stationary fluid with boundary conditions discussed in 5.3. The schematic diagram of the problem is illustrates in fig 20 (a). In fig. 21a the ellipse is at the start of upward stroke with backward motion. In fig. 21b ellipse starts an upward

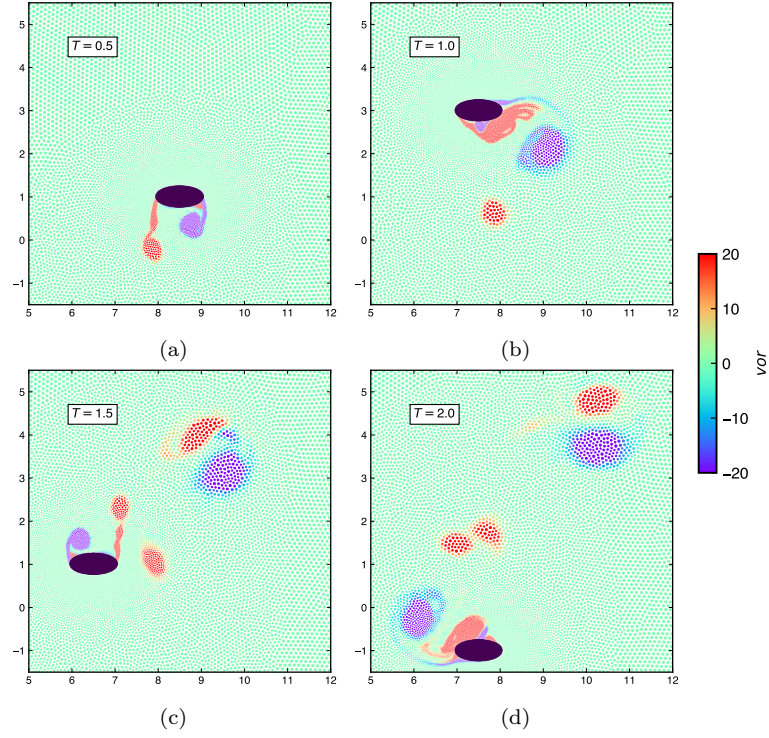


Figure 21: Vorticity distribution around the plunging ellipse at different time periods of two plunging cycles at $Re = 550$ at: (a) $T/4$, (b) $T/2$, (c) $3T/2$, and (d) T . The results are computed using solution adaptivity, with lowest resolution of $D/\Delta x_{\max} = 25$, and highest resolution of $D/\Delta x_{\min} = 100$. The point size is proportional to the mass of the particle.

stroke with a forward motion at period $T/4$. At period $T/2$, the ellipse starts the downward stroke with a forward motion. Similarly, figs. 21c and 21d show the motion of the ellipse at different time periods of $3T/2$, and T respectively.

6.3. Rotating S-shape

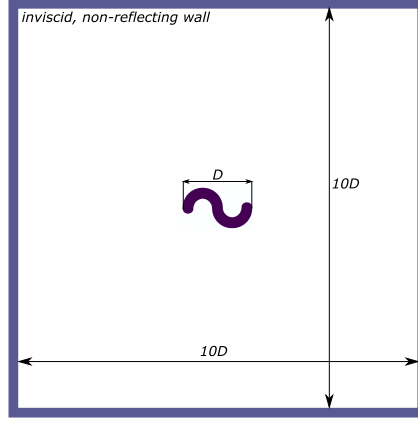


Figure 22: Schematic diagram of the rotating S-shape, where the outer diameter D of the S-shape is 2 m.

We consider a counter-clockwise rotating S-shaped body at $Re = 2000$. The outer diameter D is 2 m and fig. 22 shows the domain schematic. The minimum-resolution $D/\Delta x_{\min}$ is 10 and the maximum-resolution $D/\Delta x_{\min}$ is 200. The body is rotated at a frequency of 0.1 sec^{-1} . We simulate the problem for $t = 10 \text{ sec}$. Figure 23 shows the vorticity distribution of the particles for the rotating S-shape at $t = 2, 5, 8, 10 \text{ secs}$.

This section demonstrates the capabilities of the adaptive particle refinement in simulating complex motion and multiple bodies. This motivates further the use of adaptive EDAC-SPH in a range of applications.

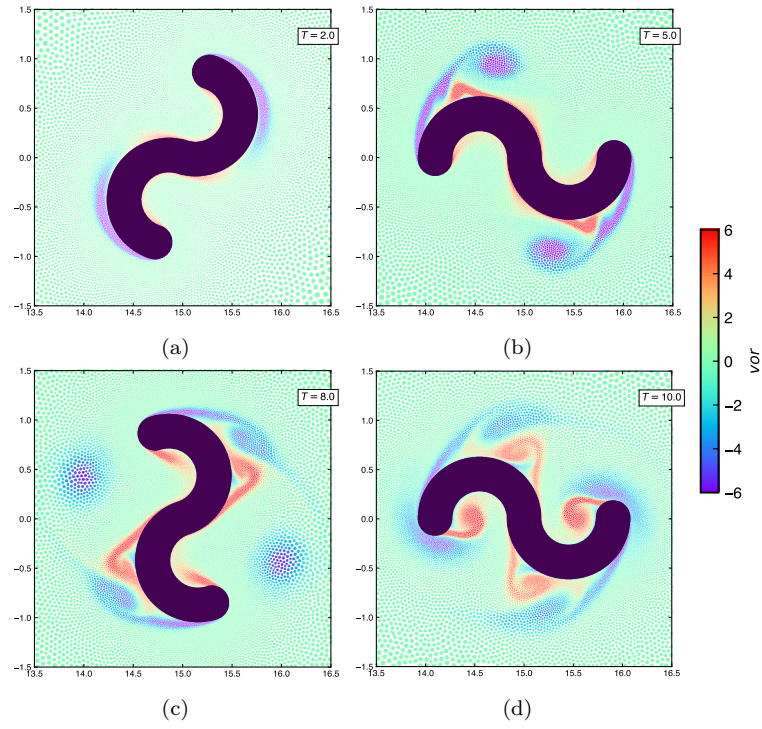


Figure 23: Vorticity distribution at different times around the counter-clockwise rotating S-shape at $Re = 2000$. The point size is proportional to the mass of the particle.

7. Conclusions

In this work a modified version of the adaptive EDAC-SPH technique of Muta and Ramachandran [1] has been discussed and various applications have been demonstrated. The adaptive particle refinement is automatic; the method is efficient in terms of the number of particles that it creates and requires an optimal number of neighbors. Besides the geometry-based automatic refinement, it is possible to create static regions of refinement or use solution-based adaptivity. Unlike the original method of [1], the proposed method does not require any background particles making it more memory efficient and easier to implement. The test cases presented in this paper clearly show the applicability and computational efficiency of the method. In particular the original method did not benchmark the method for moving bodies or for multiple bodies which we do in the current work. The results show good reliability of using adaptive particle refinement in practical applications using SPH. The proposed adaptive algorithm is executed before any SPH computations are performed at every timestep. This makes it easy to incorporate into an existing non-adaptive EDAC-SPH solver.

We show how the method can be used to simulate a variety of CFD problems that involve stationary and moving geometries of varying complexity. The source code is open-source and can be obtained from https://gitlab.com/pypr/asph_motion. It is entirely written in Python and can be made to run on different platforms, like, CPU (single and multi-core), multi-CPU, as well as a GPGPU. This makes it easy for researchers to use and extend. To our knowledge this is the only open-source code available for adaptive SPH. In the future, we propose to apply this method to other practical problems. The algorithms discussed work have not been tested for three dimensional problems and this will be investigated in the future.

Acknowledgements

We would like to thank the Aerospace Computational Engine (ACE) at the Department of Aerospace Engineering, Indian Institute of Technology Bombay for providing computational resources. We would like to thank Aditya Bhosale and Miloni Atal for the parallel Octree nearest neighbor particle search algorithm in PySPH, which was essential in the scale-up study done in this paper.

References

- [1] A. Muta, P. Ramachandran, Computer Methods in Applied Mechanics and Engineering 395 (2022) 115019. doi:<https://doi.org/10.1016/j.cma.2022.115019>.
- [2] H. H. Bui, G. D. Nguyen, Computers and Geotechnics 138 (2021) 104315. doi:[10.1016/j.compgeo.2021.104315](https://doi.org/10.1016/j.compgeo.2021.104315).
- [3] T. Ye, D. Pan, C. Huang, M. Liu, Physics of Fluids 31 (2019) 011301. doi:[10.1063/1.5068697](https://doi.org/10.1063/1.5068697).
- [4] S. J. Lind, B. D. Rogers, P. K. Stansby, Proceedings of the Royal Society A: Mathematical, Physical and Engineering Sciences 476 (2020) 20190801. doi:[10.1098/rspa.2019.0801](https://doi.org/10.1098/rspa.2019.0801).
- [5] R. Vacondio, C. Altomare, M. De Leffe, X. Hu, D. Le Touzé, S. Lind, J.-C. Marongiu, S. Marrone, B. D. Rogers, A. Souto-Iglesias, Computational Particle Mechanics (2020). doi:[10.1007/s40571-020-00354-1](https://doi.org/10.1007/s40571-020-00354-1).
- [6] D. Violeau, B. D. Rogers, Journal of Hydraulic Research 54 (2016) 1–26. doi:[10.1080/00221686.2015.1119209](https://doi.org/10.1080/00221686.2015.1119209).
- [7] M. Shadloo, G. Oger, D. Le Touzé, Computers & Fluids 136 (2016) 11–34. doi:[10.1016/j.compfluid.2016.05.029](https://doi.org/10.1016/j.compfluid.2016.05.029).
- [8] L. B. Lucy, The Astronomical Journal 82 (1977) 1013–1024. doi:[10.1086/112164](https://doi.org/10.1086/112164).
- [9] R. A. Gingold, J. J. Monaghan, Monthly Notices of the Royal Astronomical Society 181 (1977) 375–389. doi:[10.1093/mnras/181.3.375](https://doi.org/10.1093/mnras/181.3.375).
- [10] G. R. Liu, M. B. Liu, Smoothed Particle Hydrodynamics, World Scientific, 2003. doi:[10.1142/5340](https://doi.org/10.1142/5340).
- [11] J. J. Monaghan, Reports on Progress in Physics 68 (2005) 1703–1759. doi:[10.1088/0034-4885/68/8/R01](https://doi.org/10.1088/0034-4885/68/8/R01).
- [12] M. Liu, G. R. Liu, Archives of Computational Methods in Engineering 17 (2010) 25–76. doi:[10.1007/s11831-010-9040-7](https://doi.org/10.1007/s11831-010-9040-7).

- [13] D. Violeau, Fluid Mechanics and the SPH Method: Theory and Applications, 1st ed ed., Oxford University Press, Oxford ; New York, 2012. doi:10.1093/acprof:oso/9780199655526.001.0001.
- [14] J. J. Monaghan, Annual Review of Fluid Mechanics 44 (2012) 323–346. doi:10.1146/annurev-fluid-120710-101220.
- [15] L. D. Libersky, A. G. Petschek, T. C. Carney, J. R. Hipp, F. A. Allahdadi, Journal of Computational Physics 109 (1993) 67–75. doi:10.1006/jcph.1993.1199.
- [16] T. Belytschko, Y. Krongauz, D. Organ, M. Fleming, P. Krysl, Computer Methods in Applied Mechanics and Engineering 139 (1996) 3–47. doi:10.1016/s0045-7825(96)01078-x.
- [17] S. Manenti, P. Ruol, in: Proc. Int. Workshop Handling Exception in Structural Engineering, pp. 13–14.
- [18] A. Khayyer, H. Gotoh, S. Shao, Applied Ocean Research 31 (2009) 111–131. doi:10.1016/j.apor.2009.06.003.
- [19] D. Violeau, R. Issa, International Journal for Numerical Methods in Fluids 53 (2006) 277–304. doi:10.1002/flid.1292.
- [20] C. Huang, T. Long, S. Li, M. Liu, Engineering Analysis with Boundary Elements 106 (2019) 571–587. doi:10.1016/j.enganabound.2019.06.010.
- [21] X. Yang, S.-C. Kong, Computer Physics Communications 239 (2019) 112–125. doi:10.1016/j.cpc.2019.01.002.
- [22] Z.-B. Wang, R. Chen, H. Wang, Q. Liao, X. Zhu, S.-Z. Li, Applied Mathematical Modelling 40 (2016) 9625–9655. doi:10.1016/j.apm.2016.06.030.
- [23] J. J. Monaghan, Journal of computational physics 110 (1994) 399–406. doi:10.1006/jcph.1994.1034.
- [24] H. Gotoh, A. Khayyer, Coastal Engineering Journal 60 (2018) 79–103. doi:10.1080/21664250.2018.1436243.

- [25] P. K. Koukouvinis, J. S. Anagnostopoulos, D. E. Papantonis, T. E. Simos, G. Psihoyios, C. Tsitouras, in: AIP Conference Proceedings, AIP, 2009. doi:10.1063/1.3241439.
- [26] J. Monaghan, European Journal of Mechanics - B/Fluids 30 (2011) 360–370. doi:10.1016/j.euromechflu.2011.04.002.
- [27] S. Braun, L. Wieth, S. Holz, T. F. Dauch, M. C. Keller, G. Chaussonnet, S. Gepperth, R. Koch, H.-J. Bauer, International Journal of Multiphase Flow 114 (2019) 303–315. doi:10.1016/j.ijmultiphaseflow.2019.03.008.
- [28] G. Chaussonnet, T. Dauch, M. Keller, M. Okraschevski, C. Ates, C. Schwitzke, R. Koch, H.-J. Bauer, Flow, Turbulence and Combustion 105 (2020) 1119–1147. doi:10.1007/s10494-020-00174-6.
- [29] L. Wieth, K. Kelemen, S. Braun, R. Koch, H.-J. Bauer, H. P. Schuchmann, Microfluidics and Nanofluidics 20 (2016). doi:10.1007/s10404-016-1705-6.
- [30] H. Martel, P. R. Shapiro, J. V. Villumsen, H. Kang, Memorie della Societa Astronomica Italiana 65 (1994) 1061.
- [31] S. Kitsionas, A. Whitworth, Monthly Notices of the Royal Astronomical Society 330 (2002) 129–136. doi:10.1046/j.1365-8711.2002.05115.x.
- [32] M. Lastiwka, N. Quinlan, M. Basa, International Journal for Numerical Methods in Fluids 47 (2005) 1403–1409. doi:10.1002/flid.891.
- [33] Y. Reyes Lopez, D. Roose, Particle-based method II. Fundamentals and Applications (2011) 942–953.
- [34] Y. R. López, D. Roose, C. R. Morfa, Computational Mechanics 51 (2013) 731–741. doi:10.1007/s00466-012-0748-0.
- [35] F. Spreng, D. Schnabel, A. Mueller, P. Eberhard, Computational Particle Mechanics 1 (2014) 131–145. doi:10.1007/s40571-014-0015-6.
- [36] D. A. Barcarolo, D. Le Touzé, G. Oger, F. De Vuyst, Journal of Computational Physics 273 (2014) 640–657. doi:10.1016/j.jcp.2014.05.040.

- [37] S. Khorasanizade, J. M. M. Sousa, *International Journal for Numerical Methods in Engineering* 106 (2016) 397–410. doi:10.1002/nme.5128.
- [38] D. García-Senz, R. M. Cabezón, J. A. Escartín, K. Ebinger, *Astronomy & astrophysics* 570 (2014) A14. doi:10.1051/0004-6361/201424260.
- [39] P. Omidvar, P. K. Stansby, B. D. Rogers, *International Journal for Numerical Methods in Fluids* 68 (2012) 686–705. doi:10.1002/flid.2528.
- [40] W. Hu, W. Pan, M. Rakhsha, Q. Tian, H. Hu, D. Negrut, *Computer Methods in Applied Mechanics and Engineering* 324 (2017) 278–299. doi:10.1016/j.cma.2017.06.010.
- [41] L. Chiron, G. Oger, M. De Lefte, D. Le Touzé, *Journal of Computational Physics* 354 (2018) 552–575. doi:10.1016/j.jcp.2017.10.041.
- [42] J. Feldman, J. Bonet, *International Journal for Numerical Methods in Engineering* 72 (2007) 295–324. doi:10.1002/nme.2010.
- [43] R. Vacondio, B. Rogers, P. Stansby, P. Mignosa, J. Feldman, *Computer Methods in Applied Mechanics and Engineering* 256 (2013) 132–148. doi:10.1016/j.cma.2012.12.014.
- [44] J. Bonet, T.-S. Lok, *Computer Methods in applied mechanics and engineering* 180 (1999) 97–115. doi:10.1016/s0045-7825(99)00051-1.
- [45] S. Kulasegaram, J. Bonet, R. Lewis, M. Profit, *Computational Mechanics* 33 (2004) 316–325. doi:10.1007/s00466-003-0534-0.
- [46] P. Ramachandran, K. Puri, *Computers & Fluids* 179 (2019) 579–594. doi:10.1016/j.compfluid.2018.11.023.
- [47] R. Vacondio, B. Rogers, P. Stansby, *International Journal for Numerical Methods in Fluids* 69 (2012) 1377–1410. doi:10.1002/flid.2646.
- [48] R. Vacondio, B. Rogers, P. Stansby, P. Mignosa, *Computer Methods in Applied Mechanics and Engineering* 300 (2016) 442–460. doi:10.1016/j.cma.2015.11.021.
- [49] P. Ramachandran, A. Bhosale, K. Puri, P. Negi, A. Muta, A. Dinesh, D. Menon, R. Govind, S. Sanka, A. S. Sebastian, A. Sen, R. Kaushik, A. Kumar, V. Kurapati, M. Patil, D. Tavker, P. Pandey, C. Kaushik,

- A. Dutt, A. Agarwal, *ACM Transactions on Mathematical Software* 47 (2021) 1–38. doi:10.1145/3460773.
- [50] P. Ramachandran, *Computing in Science & Engineering* 20 (2018) 81–97. doi:10.1109/mcse.2018.05329818.
- [51] J. R. Clausen, *Physical Review E* 87 (2013) 013309–1–013309–12. doi:10.1103/PhysRevE.87.013309.
- [52] S. Adami, X. Hu, N. Adams, *Journal of Computational Physics* 241 (2013) 292–307. doi:10.1016/j.jcp.2013.01.043.
- [53] D. Adepu, P. Ramachandran, *arXiv e-prints* (2021). arXiv:2106.00756.
- [54] L. Hernquist, N. Katz, *The Astrophysical Journal Supplement Series* 70 (1989) 419. doi:10.1086/191344.
- [55] M. Basa, N. J. Quinlan, M. Lastiwka, *International Journal for Numerical Methods in Fluids* 60 (2009) 1127–1148. doi:10.1002/fld.1927.
- [56] P. W. Cleary, J. J. Monaghan, *Journal of Computational Physics* 148 (1999) 227–264. doi:10.1006/jcph.1998.6118.
- [57] S. Lind, R. Xu, P. Stansby, B. Rogers, *Journal of Computational Physics* 231 (2012) 1499 – 1523. doi:10.1016/j.jcp.2011.10.027.
- [58] R. Xu, P. Stansby, D. Laurence, *Journal of Computational Physics* 228 (2009) 6703–6725. doi:10.1016/j.jcp.2009.05.032.
- [59] G. Oger, S. Marrone, D. Le Touzé, M. de Leffe, *Journal of Computational Physics* 313 (2016) 76–98. doi:10.1016/j.jcp.2016.02.039.
- [60] A. J. C. Crespo, *Application of the smoothed particle hydrodynamics model SPHysics to free-surface hydrodynamics*, Ph.D. thesis, Universidade de Vigo, 2008.
- [61] S. Adami, X. Hu, N. Adams, *Journal of Computational Physics* 231 (2012) 7057–7075. doi:10.1016/j.jcp.2012.05.005.
- [62] M. Lastiwka, M. Basa, N. J. Quinlan, *International Journal for Numerical Methods in Fluids* 61 (2009) 709–724. doi:10.1002/fld.1971.

- [63] P. Negi, P. Ramachandran, *Computer Physics Communications* 265 (2021) 108008. doi:10.1016/j.cpc.2021.108008.
- [64] S. Kang, *Physics of Fluids* 15 (2003) 2486–2498. doi:10.1063/1.1596412.
- [65] Y. Bao, D. Zhou, J. Tu, *Computers & Fluids* 71 (2013) 124–145. doi:10.1016/j.compfluid.2012.10.013.
- [66] M. S. Shadloo, A. Zainali, S. H. Sadek, M. Yildiz, *Computer methods in applied mechanics and engineering* 200 (2011) 1008–1020. doi:10.1016/j.cma.2010.12.002.
- [67] M. S. Shadloo, A. Zainali, M. Yildiz, A. Suleman, *International Journal for Numerical Methods in Engineering* 89 (2012) 939–956. doi:10.1002/nme.3267.
- [68] P. Sun, A. Colagrossi, S. Marrone, M. Antuono, A. Zhang, *Computer Physics Communications* 224 (2018) 63–80. doi:10.1016/j.cpc.2017.11.016.
- [69] E. Rossi, A. Colagrossi, D. Durante, G. Graziani, *Computer Methods in Applied Mechanics and Engineering* 302 (2016) 147–169. doi:10.1016/j.cma.2016.01.006.
- [70] Sph rEsearch and engineeRing International Community, <https://www.spheric-sph.org/>, 2022. Accessed: 2022-03-25.
- [71] G. Colicchio, M. Greco, O. Faltinsen, *Proc. 21st International Workshop on Water Waves and Floating Bodies*, IWWWFB 6 (2006).
- [72] S. Marrone, A. Colagrossi, M. Antuono, G. Colicchio, G. Graziani, *Journal of Computational Physics* 245 (2013) 456–475. doi:10.1016/j.jcp.2013.03.011.
- [73] P. Koumoutsakos, A. Leonard, *Journal of Fluid Mechanics* 296 (1995) 1–38. doi:10.1017/S0022112095002059.
- [74] P. Ramachandran, *Development and Study of a High-Resolution Two-Dimensional Random Vortex Method*, Ph.D. thesis, IIT Madras, Madras, June-2004.

- [75] D. Sumner, Journal of fluids and structures 26 (2010) 849–899. doi:10.1016/j.jfluidstructs.2010.07.001.
- [76] R. Stringer, J. Zang, A. Hillis, Ocean Engineering 87 (2014) 1–9. doi:10.1016/j.oceaneng.2014.04.017.
- [77] D. C. Kolukisa, M. Ozbulut, E. Pesman, M. Yildiz, International Journal for Numerical Methods in Engineering 121 (2020) 4187–4207. doi:10.1002/nme.6436.
- [78] K. V. Rozhdestvensky, V. A. Ryzhov, Progress in aerospace sciences 39 (2003) 585–633. doi:10.1016/s0376-0421(03)00077-0.
- [79] J. Young, J. C. Lai, M. F. Platzer, Progress in aerospace sciences 67 (2014) 2–28. doi:10.1016/j.paerosci.2013.11.001.
- [80] J. Esfahani, E. Barati, H. R. Karbasian, Computers & Fluids 108 (2015) 142–155. doi:10.1016/j.compfluid.2014.12.002.
- [81] X. Wu, X. Zhang, X. Tian, X. Li, W. Lu, Ocean Engineering 195 (2020) 106712. doi:10.1016/j.oceaneng.2019.106712.